Hiroshima University

Doctoral Thesis

X-ray Study of Stellar-Wind Accretion on a Highly-Magnetized Neutron Star in a Binary System

Author:
Nagomi Uchida

Supervisor:
Dr. Hiromitsu Takahashi

A thesis submitted in fulfillment of the requirements for the degree of Doctor of Science

in the

High Energy Astrophysics Group
Department of Physical Science

September 1, 2021

HIROSHIMA UNIVERSITY

Abstract

Faculty Name
Department of Physical Science

Doctor of Science

X-ray Study of Stellar-Wind Accretion on a Highly-Magnetized Neutron Star in a Binary System

by Nagomi Uchida

An important physical parameter of neutron stars (NSs) is the strength B of their surface magnetic field (MF), because the mechanisms of their accretion and X-ray emission are strongly affected by the values of B. Accurate estimates of B of accreting NSs are available through detections of cyclotron resonance scattering features (CRSFs) in their X-ray spectra. However, the current observational sensitivity limits the CRSF detections to $\lesssim 100$ keV, and hence $B \lesssim 10^{13}$ G. As an alternative method to estimate B (particularly towards higher values) of accreting NSs, the classical accretion torque theory by Ghosh and Lamb (1979), hereafter GL79, has been revived, calibrated, and applied to several high-mass X-ray binaries (HMXBs). In particular, Yatabe et al., 2018 studied X-Persei, the HMXB which has an NS companion with a long spin period ($\sim$835 s) in an approximate torque equilibrium, a low luminosity ($\sim 10^{35}$ erg s^{-1}), and a hard continuum extending to $\sim$ 80 keV without a clear cutoff. The application of the GL79 modeling has shown that the NS in X Persei has $B \sim 10^{14}$ G, which is significantly higher than those of ordinary X-ray pulsars, and is comparable to those of magnetars. Such objects, if plenty, would challenge the consensus that magnetars are found solely as isolated NSs.

In the present study, we analyzed the best candidate of the highly magnetized NS in a binary system: IGR J00370+6122. IGR J00370+6122 is a HMXB, of which the primary is a B1 Ib star, whereas the companion is suggested to be a NS by the detection of 346-s pulsation in one-off 4-ks observation. To better understand the nature of the compact companion, the present work performs timing and spectral studies of the X-ray data of this object, taken with XMM-Newton, Swift, Suzaku, RXTE, and INTEGRAL. In the XMM-Newton data, a coherent 674 s pulsation was detected, for which the previous 346 s period may be a sub-harmonic. The spectra exhibited the “harder when brighter" trend in the 1–10 keV range, and a very flat continuum without clear cutoff in the harder 10–80 keV range. These properties are both similar to those observed from several low-luminosity accreting pulsars, including X Persei in particular. Thus, the compact object in IGR J00370+6122 is considered to be a magnetized NS with a rather low luminosity. The orbital period was refined to 15.6649 ± 0.0014 d. At the orbital phases 0.3 (and probably vice versa at 0.95), the luminosity suddenly drops from 4×10^{33} to $< 1 \times 10^{32}$ erg s^{-1}, beyond what is predicted by the Hoyle-Lyttleton accretion from primary’s stellar winds. This phenomenon can be explained by the propeller effect with a strong MF of $> 5 \times 10^{13}$ G. Therefore, the NS in IGR J00370+6122 is suggested to have a stronger dipole MF, compared to ordinary X-ray pulsars.

Contents

List of Figures

Chapter 1

Introduction

Stars are spherical objects which are supported by some type of inner pressure against gravitational compression. A difference of the inner pressure, which depends on stellar equations of state, determines their strictures. We can employ four types of pressure for a supporting power of the stars, i. e. Coulomb repulsion, electron degeneracy pressure, classical gas pressure, and neutron degeneracy pressure. In the case of planets like the Earth and Jupiter, the pressure which works against the gravitational pressure is the Coulomb repulsion. For main sequence stars like the Sun and Vega, the classical gas pressure plays a role of repulsive force. The electron degeneracy pressure is mainly working in brown dwarfs and white dwarfs. Neutron stars (NSs), which are protagonists of this thesis, are supported by the degeneracy pressure of neutrons.

In 1934, Baade and Zwicky predicted the existence of NSs following a discovery of uncharged particles, i. e. neutrons, by James Chadwick in 1932. A first discovery of an NS was made in 1967 by Antony Hewish and Jocelyn Bell. This was observed as periodic radio pulses with the period of $\sim$1.3 s. So far, about 3000 NSs were catalogued on the pulsar catalog of the Australia Telescope National Facility (ATNF). Current understandings of the NS's natures are followings.

- Most of the NSs are found in the Galactic plane.
- Typical radius: $10-12$ km
- Typical mass: $\sim 1.4\ M_\odot$ (Theoretical upper limit $\sim 3M_\odot$)
- Spin period: 1.5 ms-10^7 ms
- Surface Magnetic field: $10^8 - 10^{15}$ G
- There are roughly two types of emission mechanisms, i. e. rotation-powered and accretion-powered.
- The emissions are aligned by their strong magnetic fields (MFs) and a misalignment of the NS's spin and magnetic axes causes the periodic signals.

However, the extreme conditions, e. g. the strong MFs, fast spin period, and strong gravitational field, block the way to understand the properties of the NSs. We still have a lot of mysteries for their birth, characteristics, radiation process, and gravitational wave. One of the most mysterious characteristics of NSs is their MFs. NSs with the strong MFs of $\gtrsim 10^{14}$ G are generally called Magnetars.

Interestingly, magnetars are only found as isolated systems (not in binary systems) and the reason is still unknown. We cannot ignore the selection effect due to the observational difficulty of magnetars in binary systems. For isolated NSs, we can simply estimate their surface MFs by assuming the magnetic dipole radiation. This

method is not applicable to the accretion-driven systems since angular momentum is transported from a companion star to a NS. We employ absorption-like features on their X-ray spectrum, which are proportional to MF strength, instead of the magnetic dipole radiation for the MFs estimation of binary systems. However, this method is limited for the MFs of $<10^{13}$ G since this spectral feature appeared >100 keV for the MFs of $>10^{13}$ G.

In the present study, we applied a new estimation method of NS's MF, accretion torque model, for a binary system and reveal that the possible presence of a highly magnetized NS in a binary system.

This thesis consists of seven chapters. First, we introduced the fundamental characteristics and recent topics of NSs in chapter 1. Next, the scientific motivations of this research were explained in chapter 2. Chapter 3 reviews satellites and instruments we employed in this research. Then, all analyzed data and data reduction techniques are explained in chapter 4. In chapter 5, we performed the spectral and timing analysis for all exist data of a target star. We discussed the accretion mechanism and MF of the NS in chapter 6. Finally, we conclude the obtained scientific results and the future prospects of this study in chapter 7.

1.1 Neutron Star Overview

Neutron Stars (NSs) are the stars which are supported by their degenerate pressure of neutrons. Their mass and radii are about $1.2 - 2.0 M_{\odot}$ and ~ 10 km, respectively. This was theoretically predicted by Baade and Zwicky (Baade and Zwicky, 1934) in the context of the discovery of neutrons in 1932. In 1967, Antony Hewish and Jocelyn Bell found periodic signals from a data of a radio telescope, and this was later confirmed as a "radio pulsar" which is one of the classes of the NSs. A bunch of NSs is reported so far. Most of the NSs have strong MFs of $B \sim 10^{11}$ G and this causes a beam-like radiation emission from this magnetic pole. The observed pulsed emission can be caused by a misalignment of the magnetic pole and the rotation axis.

NSs are born as the final stage of the star evolution process, so-called Type-II supernovae. Massive stars, of which the mass of $\gtrsim 8 M_{\odot}$, grow up through CNO-cycle and formed iron core. NSs (or black holes) are born in the gravitational collapse triggered by iron-core instability. If NSs are born alone, this is the final state of the stellar evolution, and they are cooling and spinning down rapidly with their efficient thermal conductivity due to the neutron degeneracy and the magnetic dipole radiation. However, if the NSs are gravitationally captured by another star, OB-type or GKM-type star, it will start to grow and spinning up again by mass transfer (pulsar recycled scenario). The brief history of NSs life was presented in FIGURE 1.1. The interactive mass transfer drastically changes their life and NS classifications. Therefore, the understanding of the NS feature is significantly important for the stellar evolution scenario.

The radiation emission processes can be a good method to classify the NSs. Magnetars are thought to be younger NSs compared to others. They have extremely strong B of $\gtrsim 10^{14}$ G, and so-called Magnetar, and emit X-ray and Gamma-ray by magnetic dipole radiation. The majority of NSs are classified as radio pulsars of isolated NSs or millisecond pulsars in binary systems. They are observed mainly in radio band (sometimes in X-ray and Gamma-ray bands) with converting their rotational energy into the magnetic dipole emission. X-ray Pulsars and Low-Mass X-ray binaries (LMXBs) are the second-most populous in the NS zoo. They are the binary systems which consist of NSs with early-type (OB-type) stars or late-type (GKM-type) stars,

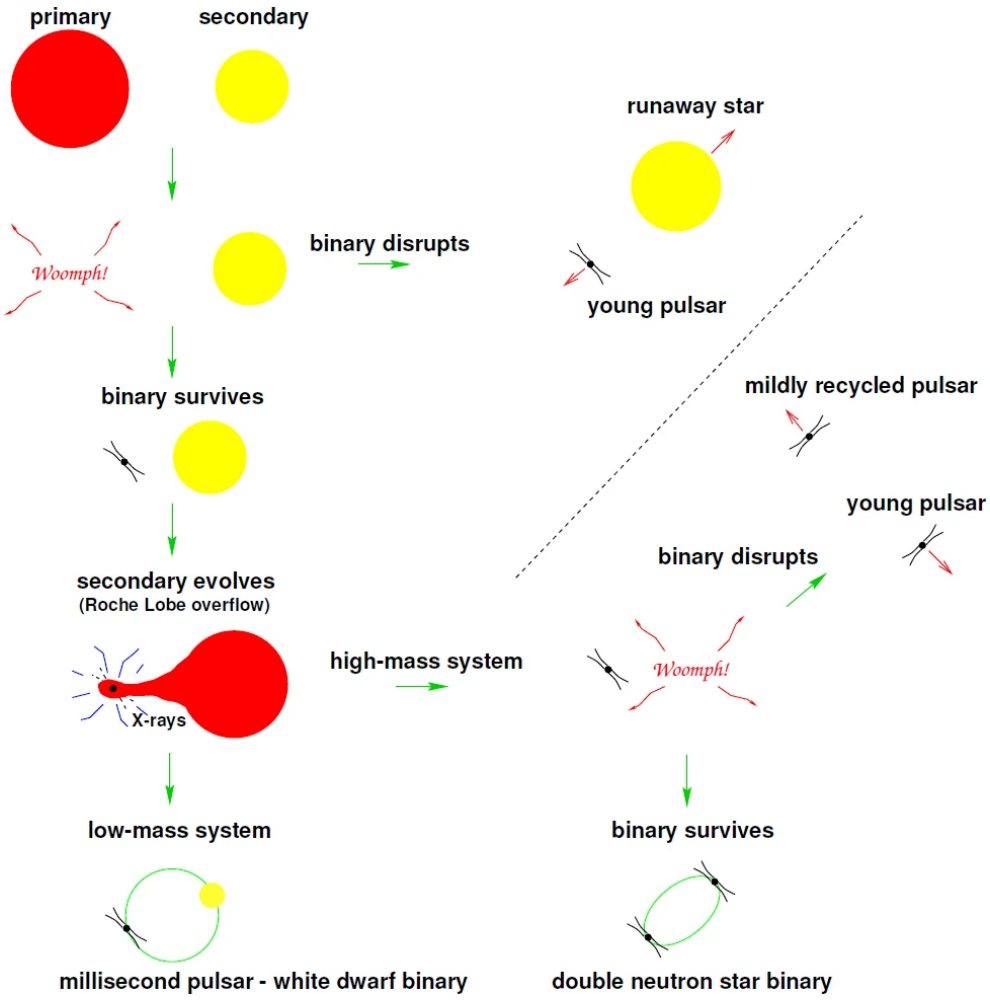

FIGURE 1.1: Binary system evolution with NSs (Faber and Rasio, 2012)

.

respectively. In this case, NSs gravitationally capture the star wind of early-type stars or the surface layer of late-type stars and such accretion matter releases the gravitational energy and emits the radiation in the X-ray band. The rare classifications of the NSs are Central compact objects (CCOs) and X-ray dim isolated NSs (XINSs). Only about 10 sources were reported for as these classifications and not understood well yet. The spectral features indicate the thermal emission in soft X-ray. These classifications and radiation emission mechanisms are shown in TABLE 1.1.

TABLE 1.1: NS Classification by their radiation process.(Fumio T. et al., 2020)

Emission process	Isolated	Binary	Observation band
Rotational	Radio pulsar	Radio (millisecond) Pulsar	(Mainly) Radio
Thermal	CCO, XINS	–	Soft X-ray
Gravitational	–	X-ray Pulsar, LMXB	X-ray
Magnetic	Magnetar	–	X-ray, Gamma-ray

1.2 Isolated Neutron Stars

The isolated NSs mainly emit the radiation in the radio band by using their rotation energy. Their spin period P and spin derivative $\dot{P} = dP/dt$ are often used to characterize their habits and habitats since we can roughly estimate their ages and MF strengths.

By assuming a NS as a rotating spherical rigid body, a rotation energy $E_{\rm rot}$ and energy loss $\dot{E}_{\rm rot}$ by the spin-down can be written in below by using the angular frequency $\Omega = 2\pi/T$ and inertia momentum I.

$$E_{\rm rot} = \frac{1}{2} I\Omega^2 = 2\pi^2 I P^{-2} \tag{1.1}$$

$$\dot{E}_{\rm rot} = \frac{dE_{\rm rot}}{dt} = -4\pi^2 I P^{-3}\dot{P} \tag{1.2}$$

Then, the age of the NS can be roughly estimate as $\tau \sim -E/\dot{E} = P/2\dot{P}$ by using equation 1.1 and 1.2. In the case of Crab pulsar, which is one of the most famous isolated NSs, the age of $\tau \sim 1300$ yr was calculated by using their spin period and spin down rate as $P = 34$ ms and $\dot{P} = 4 \times 10^{-13}$ s s^{-1}, respectively.

Next, we can define two specific luminosities, i. e, spin down luminosity $L_{\rm rot}$ and magnetic dipole radiation $L_{\rm mag}$ in a vacuum.

$$L_{\rm rot} = -\frac{d}{dt}\left(\frac{1}{2} I\Omega^2\right) = -I\Omega\dot{\Omega} = \frac{(2\pi)^2 I\dot{P}}{P^3} = 3.95 \times 10^{46} \left(\frac{\dot{P}}{1\ {\rm s/s}}\right)\left(\frac{P}{1\ {\rm s}}\right)^{-3} \tag{1.3}$$

$$L_{\rm mag} = \frac{2}{3}\frac{\mu^2\Omega^4}{c^3}\sin^2\alpha \tag{1.4}$$

By equating the equation 1.3 and 1.4, we obtained the surface MF B as below.

$$B = \mu/R_{\rm NS}^3 = 3.2 \times 10^{12}\ {\rm G} \left(\frac{\dot{P}}{10\ {\rm s/s}}\right)\left(\frac{P}{1{\rm s}}\right) \tag{1.5}$$

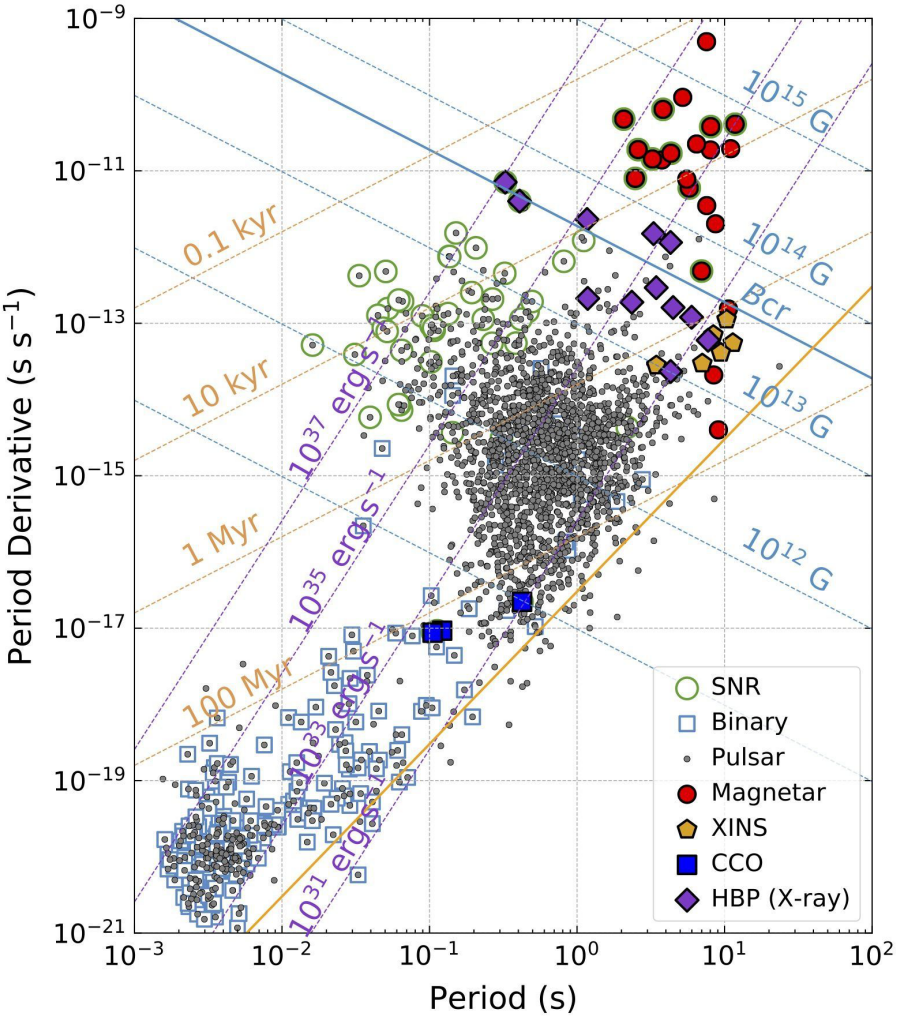

FIGURE 1.2: $P-\dot{P}$ diagram adapted from Enoto, Kisaka, and Shibata, 2019.

FIGURE 1.2 is the NSs distribution in the $P-\dot{P}$ space, so-called $P-\dot{P}$ diagram. This indicates the large diversity of NSs. The supernova-originated NSs are born at the upper left part of the FIGURE 1.2. The NSs move to the right bottom direction with pinning down and decreasing $L_{\rm rot}$ as the NSs get older. The yellow solid line in FIGURE 1.2 is called "death line" and this indicates that $L_{\rm rot}$ become lower than $\sim 10^{30}$ erg/s and hard to observe for us. Once the NSs die by passing through the death line, the NSs cannot observe so far. However, if the NSs get companions and feed their mass via wind/disk accretion, they can get the angular momentum and start spinning up again. Finally, they revive from the pulsar grave and appeared in the left bottom part of the FIGURE 1.2 as a millisecond pulsar. This recycled scenario is well supported with the distribution in $P-\dot{P}$ diagram.

1.3 Neutron Stars in Binary Systems

The binary systems are important for understanding the evolution of NSs. They emit X-ray by mass accretion from main sequence stars, i. e., optical stars. The binary systems which consist of NSs and main sequence stars can be divided into two classes by the mass, i. e. spectral type, of the optical stars since their different accretion

process and X-ray behavior. If the optical companions are early-type (OB-type) stars, these systems are called high-mass X-ray binaries (HMXBs), while the low-mass X-ray binaries (LMXBs) for the late-type (GKM-type) stars. Some of the X-ray binaries are classified as symbiotic X-ray binaries (SyXB), which are the binaries with red giants, and they tend to have a longer spin and orbital periods.

The X-ray pulsation is expected for both HMXBs and LMXBs if the NS is magnetized strongly since the accretion material falls on the magnetic pole along with their MF (X-ray pulsar). However, many of the X-ray pulsars are classified as HMXBs since the MF become weakened with their age.

There is a relationship between the orbital period and the mass of the optical star, while the NS spin period is related to the interaction between the accretion material and MF. Therefore, we can classify the X-ray pulsars by plotting the pulse period for their orbital period (FIGURE 1.3).

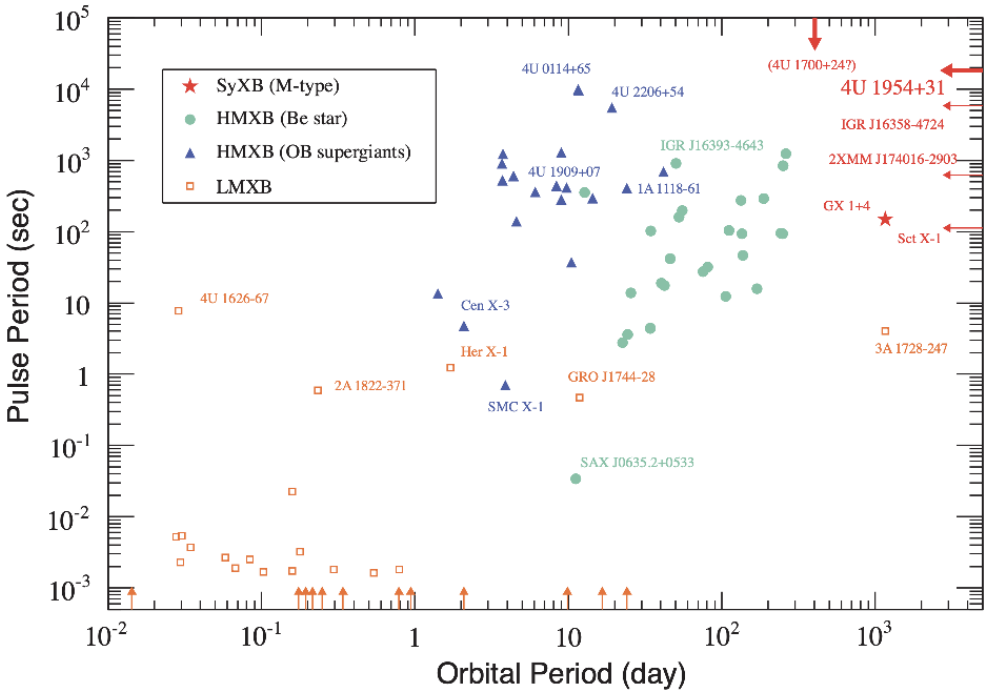

FIGURE 1.3: Corbet diagram adapted from Enoto et al., 2014

1.3.1 Low-Mass X-ray Binaries

LMXB is a binary system which mainly consists of a late-type star and neutron star or black hole (BH). Most of the NSs in LMXBs have weak MF of $< 10^{10}$ G and locate around the Galactic bulge and globular clusters since these systems are relatively older. The optical stars are filling their Roche-lobe and the overflowing gas move to NSs via a Lagrangian point L_1 (see FIGURE 1.4).

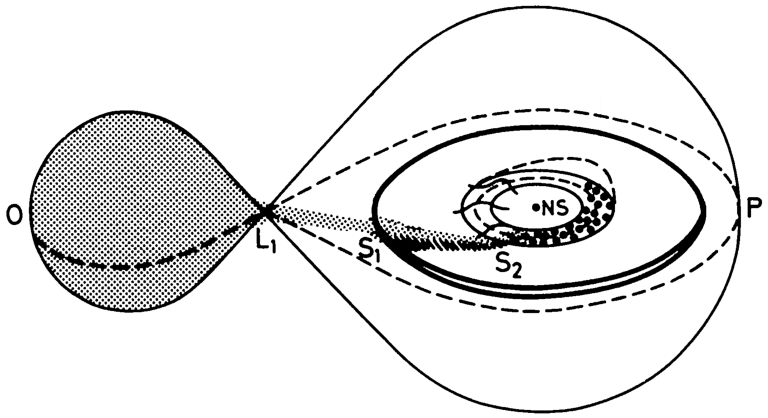

FIGURE 1.4: Geometrical structure of LMXBs illustrated in Frank, King, and Lasota, 1987.

The overflowing gas, which passes through the L_1, formed an accretion disk. The gravitational energy is released at the inner part of the disk or the NSs surface, and then emits the radiation in the X-ray band. The radiation is generated in the optically thick plasma and the resultant X-ray represents the blackbody spectrum in the case of bright objects. The spectral shape is drastically changed by the accretion rate and the disk condition.

The gas which reached the NSs surface causes nuclear fusion and forms He. The generated He pool on the NSs surface sometimes caused the nuclear burst and was observed as an X-ray transient (X-ray burst). These X-ray bursts were only observed for the NSs binary since the BHs do not have the surface. Therefore, this X-ray burst can be a discriminant for the compact star in LMXBs. Some of the NSs in LMXBs are observed as millisecond pulsars and this strongly supported the pulsar recycle scenario.

1.3.2 High-Mass X-ray Binaries

HMXBs are the binaries which consist of the early-type (OB-type) stars and NSs or BHs. The Roche lobe is not filled in this system, while the strong stellar wind is directly brought onto the NS surface (see FIGURE 1.5). Therefore, the accretion mechanism of HMXBs is completely different with the LMXBs case.

The accretion gas is trapped by the strong NS's MF at the point which the accretion pressure (ram pressure) and the magnetic pressure are well balanced. This is called Alfvén radius and can be written in below.

$$\begin{aligned} R_{\rm A} &= \left(\frac{B^2 R_{\rm NS}^6}{2\dot{M}\sqrt{2GM_{\rm NS}}}\right)^{2/7} \\ &\approx 2.5\times10^8 \left(\frac{R_{\rm NS}}{10^6\ {\rm cm}}\right)^{12/7} \left(\frac{B}{10^{12}\ {\rm G}}\right)^{4/7} \left(\frac{\dot{M}}{10^{17}\ {\rm gs}^{-1}}\right)^{-2/7} \left(\frac{M_{\rm NS}}{M_\odot}\right)^{-1/7} [{\rm cm}] \end{aligned} \tag{1.6}$$

Here, $\dot{M}$, $M_{\rm NS}$, and B are the accretion rate, mass of NS, and surface MF strength, respectively. The accretion matter, which reaches on the Alfvén radius, is trapped by the NS's MF and falls onto the magnetic pole of the NS along the MF line (see FIGURE 1.6). This is called an accretion column and most of the X-rays are generated around the shock surface formed near the NS surface in this accretion column.

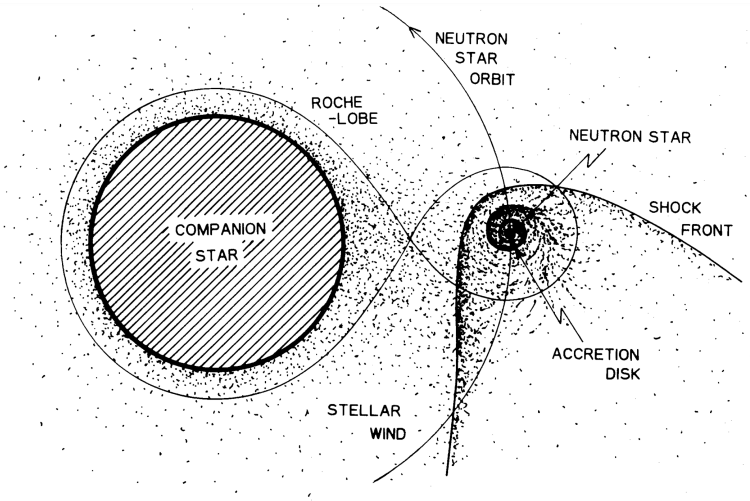

FIGURE 1.5: Geometrical structure of HMXBs illustrated in Nagase, 1989.

Some HMXB shows the line emission in their optical spectrum, thus classified as B"e"-type star, and this indicates that the existence of circumstellar disks. They have a longer orbital period and larger eccentricity than ordinal OB-type ones. In this case, the mass transfer is driven by a disk overflow.

1.3.3 Supergiant Fast X-ray Transients

Supergiant Fast X-ray Transients are thought to be one of the classifications of HMXBs. Most of SFXTs, $\sim$ 10 objects, are discovered as the X-ray transients by the INTEGRAL satellite in hard energy band >17 keV. The spectral type indicates that their optical counterparts are supergiants. Some of them show the elusive pulsations only in their X-ray outbursts. The characteristics of SFXTs are simply organized with three features by Sidoli, 2017 as follows.

1. Low duty cycle ($\lesssim$5%) in bright X–ray flares (at $L_X \gtrsim 10^{36}$ erg s^{-1})
2. High dynamic range (ratio between maximum and minimum X–ray luminosity) $\gtrsim$100
3. Low time-averaged luminosity $L_X \lesssim 10^{34}$ erg s^{-1}

The long quiescent states, which compare to the time of X-ray burst, caused the difficulty of the observational research, and this refracted as a few numbers of observations, i.e., $\sim$ 10 objects. The origin of the drastic luminosity change is still unknown in spite of a decade year from the first report of a SFXT. There are three main theories to explain the origin of the strong flaring activity: (1)an eclipse, (2)a clumpy stellar wind, and (3)magnetic gating(Romano et al., 2010, Romano et al., 2012, Ducci, L. et al., 2013, Bozzo, Falanga, and Stella, 2008). The typical SFXTs explained by their three theories are IGR J18483−0311, IGR J17354−3255, and IGR J16418−4532. IGR J18483−0311 has an orbital period of 18.5 days, while those of IGR J17354−3255 and IGR 16418−4532 are 8.4 days and 3.7 days, respectively.

All of the orbital folded light curves had a quiescent phase, and three models were proposed to explain the dip behavior: (1) an eclipse, (2) the propeller effect, and (3) a clumpy stellar wind. IGR J16418−4532 was by (1) and IGR J17354−3255 was by (1) or (2). IGR J18483−0311 had all possibilities. However, these are locating close to

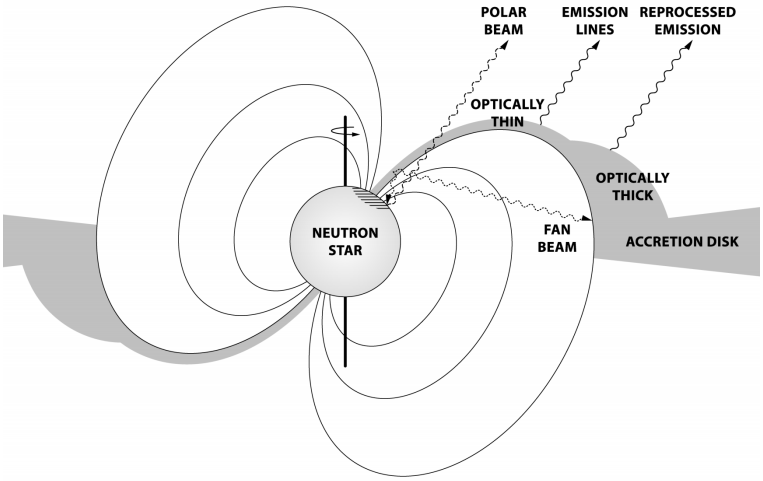

FIGURE 1.6: Schematic representation of the accretion region illustrated in Koliopanos, Filippos and Vasilopoulos, Georgios, 2018.

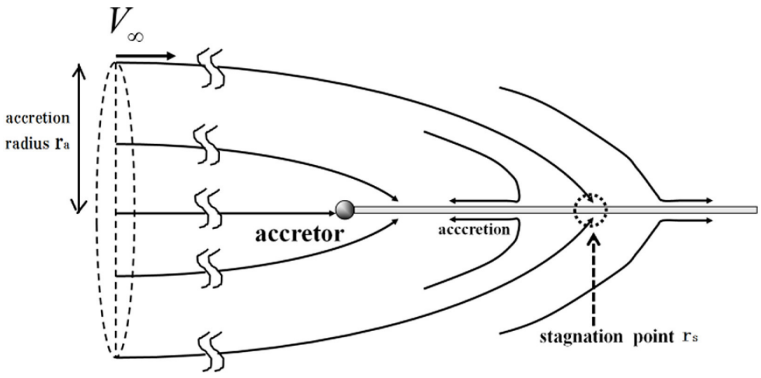

FIGURE 1.7: Schematic representation of Hoyle-Lyttleton accretion adapted from Ohsugi, 2018.

the center of the Galaxy. The strong galactic absorption causes the poor constraint on the X-ray emission mechanisms and the MF structures for these SFXTs.

1.3.4 Wind Accretion theories for HMXBs

A theory of the accretion onto the compact object, i. e. NS or BH, is proposed by Hoyle and Lyttleton in 1939(Hoyle and Lyttleton, 1939). This is a basic theory of the accretion process and so-called Hoyle-Lyttleton accretion. The effective radius of NS's gravitational field for the accretion material was calculated in this model. The brief schematic of the Hoyle-Lyttleton accretion is shown in FIGURE Ohsugi, 2018.

Here, we assumed the compact object (NS or BH) with the mass M is passing through the space, which is filled with uniform gas, with the speed of v_∞. The gas in the radius of $R_{\rm HL}$ should be drawn into the compact object, while the gas of the outer part $> R_{\rm HL}$ should stay without affected by gravity. Then, this radius $R_{\rm HR}$ is called Hoyle-Lyttleton accretion and can be written in below.

$$R_{\rm HL} = \frac{2GM}{v_\infty^2} \sim 2.65 \times 10^{15} \frac{M}{10M_\odot} \left(\frac{v_\infty}{19 {\rm kms}^{-1}}\right) \tag{1.7}$$

G is the gravitational constant.

The mass accretion rate is also defined in below.

$$\dot{M}_{\rm HL} = \pi R_{\rm HL}^2 \rho_\infty v_\infty = \frac{4\pi\rho_\infty G^2 M^2}{v_\infty^3} \tag{1.8}$$

In the Hoyle-Lyttleton accretion theory, a stable and uniform accretion gas is assumed. However, the density and velocity of the stellar wind should be changed by the location of the NS on the orbit since these parameters strongly depend on the distance from the massive star and orbital eccentricity. In addition, a relative velocity between the orbital and wind velocity. We can simply assume this effect by replacing v_∞ with the relative velocity $v_{\rm rel} = v_{\rm w}^2 + v_{\rm orb}^2 + 2v_{\rm w}v_{\rm orb}{\rm cos}\theta$ (Raguzova and Lipunov, 1998). Here, $v_{\rm w}$, $v_{\rm orb}$ and θ are a wind velocity orbital velocity and an angle between these two vectors. The wind velocity is sometimes measured by optical spectrum and we can directly substitute the measured values to $v_{\rm w}$.

However, this is the simplest case of wind accretion and the slight difference will be caused in the case of disk-accreting and/or high-luminous (close to Eddington luminosity) systems.

1.3.5 Accretion onto the rotating and highly magnetized NS: Propeller effect

For binary X-ray pulsars, three typical radii are used to characterize the accretion physics. Two of them are already described in the previous sections, i. e., Hoyle-Lyttleton accretion (equation 1.7) and Alfvén radius (equation 1.7). Finally, we can define a corotation radius $R_{\rm co}$ as below.

$$R_{\rm co} = \left(\frac{GM_{\rm NS}}{\omega^2}\right)^{1/3} \tag{1.9}$$

Here, $\omega = 2\pi P$ is the angular velocity of the NS. This radius indicates that the distance where the Keplerian speed of the accretion material equals the rotation speed of the NS.

For highly magnetized NSs, $R_{\rm A}$ becomes larger than $R_{\rm co}$, i. e., the magnetic pressure becomes larger than the accretion pressure. In this case, the accretion materials are blown away by the centrifugal force (see FIGURE 1.8). This is called "propeller effect" and the luminosity is rapidly dimmed or disappeared in this regime.

This mode transition can occur in both the wind accretion and disk accretion. The luminosity change for the usual disk accretion is stable than the case of wind-accretion since the disk behaves as a regulator of the accretion rate. Therefore, some of the luminosity changes, which were explained by the mode transitions, were reported for the disk accretion while a few reports for the wind-accretion system. The rapid luminosity-extinctions were observed for Aql X-1, the LMXB with the NS companion, and explained by the mode transition from the accretion to propeller regime(Matsuoka and Asai, 2013; Asai et al., 2013).

1.4 Magnetic field estimation

For NSs, their mass, radius, and surface MF strength are important physical parameters to investigate the X-ray emission mechanism and constrain on the nuclear equation of states. The surface MF of the isolated NS can be estimated by $\dot{P}$ and its luminosity by equation (1.5). However, the situation is drastically different for the

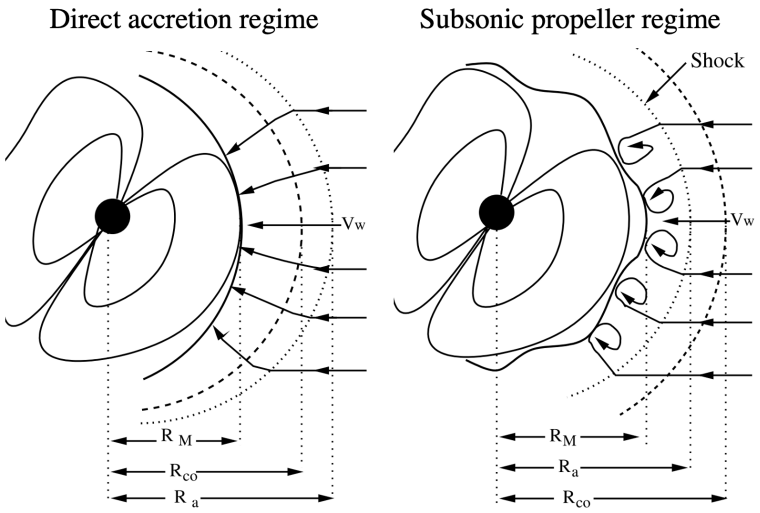

FIGURE 1.8: Schematic representation of propeller effect adapted from Bozzo, Falanga, and Stella, 2008. Left panel illustrate the accretion mode while the propeller mode for right panel.

binary systems. The angular momentum of the accretion material should be given to the NS for the case of binary systems. The spin-down rate should not correspond in one-to-one. The estimation of the surface MF of NSs in binary systems is difficult and there are still few reports on this field. There are two methods are proposed for estimating the MF of the binary systems. One is the method using the absorption-like feature in the spectrum, which is called Cyclotron Resonance Scattering Feature (CRSF), proportional to their MF strength. This is a well-established method and is widely used for some X-ray binaries. However, this method is limited to the MF of $<10^{13}$ Gauss with the current observation sensitivity, where CRSFs appear over 100 keV. Recently, as another method to estimate the MF, the accretion torque theory proposed by Ghosh &Lamb in 1979 (Ghosh and Lamb, 1979; hereafter GL79) was calibrated and applied for several HMXBs (Makishima, 2016; Sugizaki et al., 2017; Yatabe et al., 2018).

1.4.1 Cyclotron Resonance Scattering Feature

The CRSF is a classical, but powerful method to estimate the MF strength of the binary X-ray pulsars. In the strong MF, the momentum of electrons is quantized and limited to have the discrete value (Landau level). Photons, which have the equivalent energy with landau level, are absorbed and excite the electrons when passing through the magnetically pinned plasma. The excited photons return to the ground level with emitting the photons of corresponding energy, immediately. Phenomenologically speaking, the photons, in which the energies are landau level, are scattered by MF of the NS. This effect is observed as some absorption-like features on the spectrum (see FIGURE 1.9).

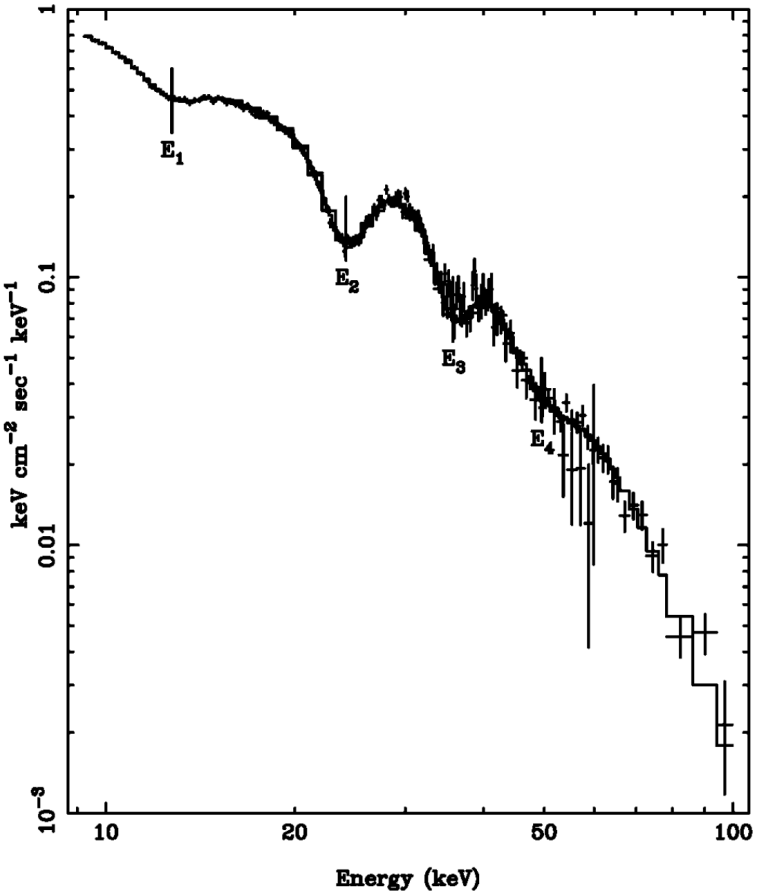

FIGURE 1.9: The unfolded spectrum of X0115+63 (Santangelo et al., 1999). 1st to 4th harmonics are significantly appeared in this spectrum.

The energy, which the absorption-like feature appeared, can be described as below.

$$E_{\rm n} \simeq 11.6\ {\rm n} \left(\frac{\rm B}{10^{12}\ {\rm G}} \right) [{\rm keV}] \qquad ({\rm n} = 1, 2, ...) \tag{1.10}$$

The CRSF was firstly observed from Her X-1 in 1976 (Truemper et al., 1978). They used the scintillation balloon-borne detector consists of NaI scintillator and successfully observed the CRSF around 40 keV. This feature was reconfirmed by Suzaku, and their MF strength was accurately calculated as $(2.9 \pm 0.3) \times 10^{12}$ G (Mihara et al., 1990). These features have been observed for ~ 20 binaries, so far. However, CRSFs are not so steep line and sometimes hard to determine whether the feature is an emission line or the absorption, e. g. X-Persei. The most important limit for using the CRSFs as a Tesla meter is the detection sensitivity of X-ray. The CRSF appears over 100 keV for $\sim 10^{13}$ G and it is hard to measure due to the X-ray detection efficiency of the current device. Therefore, we cannot apply this method for the highly-magnetized NSs.

1.4.2 Accretion Torque Model

In this method, we can estimate the MF strength, radius, and mass using the luminosity and NS spin period derivative ($\dot{P}$) by assuming the torque equilibrium. When the gravitational pull and magnetic pressure working to the accretion matter are well balanced, the $\dot{P}$ value is derived as a function of NS mass $M_{\rm NS}$, NS radius $R_{\rm NS}$, the

angular velocity of the accretion gas at the Alfvén radius $\omega_{\rm K}$, the angular frequency of NS $\Omega_{\rm NS}$, the magnetic moment of NS μ, the inertia moment of NS J and X-ray luminosity $L_{\rm X}$.

$$-\frac{\dot{P}}{P^2} = f\left(M_{\rm NS}, R_{\rm NS}, \frac{\Omega_{\rm NS}}{\omega_{\rm K}}\right)\mu^{2/7}J^{-1}L_{\rm X}^{6/7} \tag{1.11}$$

In the case of $\Omega_{\rm NS}/\omega_{\rm K} < 1$, the NS is spinning up by the accretion, while $\Omega_{\rm NS}/\omega_{\rm K} > 1$, NS is spinning down by the propeller effect. Assuming the torque equilibrium in the binary system, f is vanished since $\dot{P}$ is zero. The equation for the torque equilibrium condition can be expressed as

$$B \sim 1.8\times10^{12}\zeta^{-7/4}\left(\frac{L_{\rm X}}{10^{30}\ W}\right)\left(\frac{P}{1{\rm s}}\right)^{7/6}\ [{\rm G}] \tag{1.12}$$

where $\eta \sim 1$ is a numerical factor. The GL79 model was applied to a HMXB: X-Persei, which has a NS companion showing both spins up and down (i.e., the torque equilibrium) with a long spin period ($\sim$ 835 s) and low luminosity ($\sim 10^{35}$ erg/s). The results predicted the presence of an accretion-powered pulsar with a strong MF ($\sim 10^{14}$ G) which is comparable to magnetars (Yatabe et al., 2018). This is due to the slower spin and fainter luminosity than typical HMXBs with 10^{12} G. Since X Persei is the first HMXB candidate with $\sim 10^{14}$ G, it is important to discover another strongly magnetized candidate with a long spin period in faint HMXBs. However, the GL79 model assumes the case of disk accretion, and the applicability of the model to the wind accreting system is still unknown since the efficiency of the angular momentum transport is more complex than the case of disk accretion. There are no application examples. The applicability of the GL79 model for the wind accretion system arrows us to efficiently find the highly-magnetized NS in binary systems.

1.4.3 Quasi-spherical accretion

The slow spin period and the low luminosity can be good signs of highly-magnetized NS as predicted by GL79. One of the SFXT called IGR J11215−5952 was thought to be a strong MF because of its slow spin period ($P_{\rm spin}$ = 187 s, Swank, Smith, and Markwardt, 2007) and low luminosity ($< 3.7\times10^{33}$ erg s^{-1} in quiescent and 1.1×10^{36} erg s^{-1} in outburst, Romano et al., 2007). However, a CRSF was not found on its spectra, and this suggests that the NS possibly has relatively weak MF ($< 10^{11}$ G) or extremely high MF ($> 10^{13}$ G). A quasi-spherical accretion (QSA) theory was proposed to explain the slow spin period and low luminosity without invoking the strong MF. The accretion matter accretes via quasi-spherical shell, which was formed inside $R_{\rm HL}$, while in the case of disk accretion. The matter can be convectively settled down to the subsonic range, and the angular momentum per unit accretion mass, which is brought into the NS, is less than in the case of the disk accretion (figure 1.10).

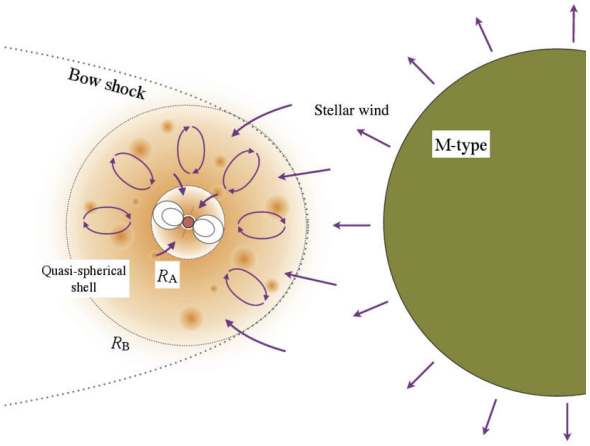

FIGURE 1.10: A simple illustration of quasi-spherical accretion adapted from Enoto et al., 2014. The accretion matter is settled down in a quasi-spherical shell formed between the Alfvén radius (R_A) and Hoyle-Lyttleton radius (R_B).

Consequently, the slow spin period with the low luminosity can be explained without invoking the strong MF. In addition, a drastic luminosity fluctuation, which is observed in some SFXTs, can be understood to be due to the accretion material accumulated during the quiescent phase falling on the NS at the periastron. Enoto et al., 2014 and (Sidoli et al., 2020) explained the pulse profile and slow spin period of 4U 1954+319 (HMXB) and IGR J11215−5952 (SFXT) by the QSA model. In some cases, as seen in 4U 0114+65, magnetar-like MFs were estimated, even if the QSA model was applied, due to its extremely long rotation period (Sanjurjo-Ferrrín et al., 2017). The QSA model is still not understood well because of the poor application.

1.5 Nature of the X-ray spectrum

The spectra of typical X-ray pulsars are shown in figure 1.11. Most of the X-ray spectrum of X-ray pulsars is reproduced by a power-law with an exponential cutoff. A hard X-ray emission extended above $\sim$ 100 keV without any cutoff feature was reported for some X-ray pulsars. Many of the spectra are well reproduced by the `compmag` model. This model assumes a cylindrical accretion onto a magnetized NS. In this model, seed photons, which were generated by blackbody radiation generated near the NS surface, were inverse-Comptonized inside the accretion column. `compmag` is a model that is widely used to fit the emission from the accretion column. This model is (Farinelli et al., 2012). A Negative and positive power law with exponential cutoff (NPEX) model is also widely used to fit spectra of X-ray pulsars Mihara, 1995; Makishima et al., 1999. Blackbody radiation, bremsstrahlung radiation, and cyclotron radiation are discussed as the origin of the seed photons. However, no model can provide a unified interpretation of the X-ray pulsar spectrum so far.

1.5.1 Spectral features of HMXBs in the low luminous state

Some HMXBs have characteristic structures and behaviors in their spectrum at a low luminous state. In the following, these interesting spectral features are explained. Note that these phenomena are not understood theoretically enough because of fewer observations.

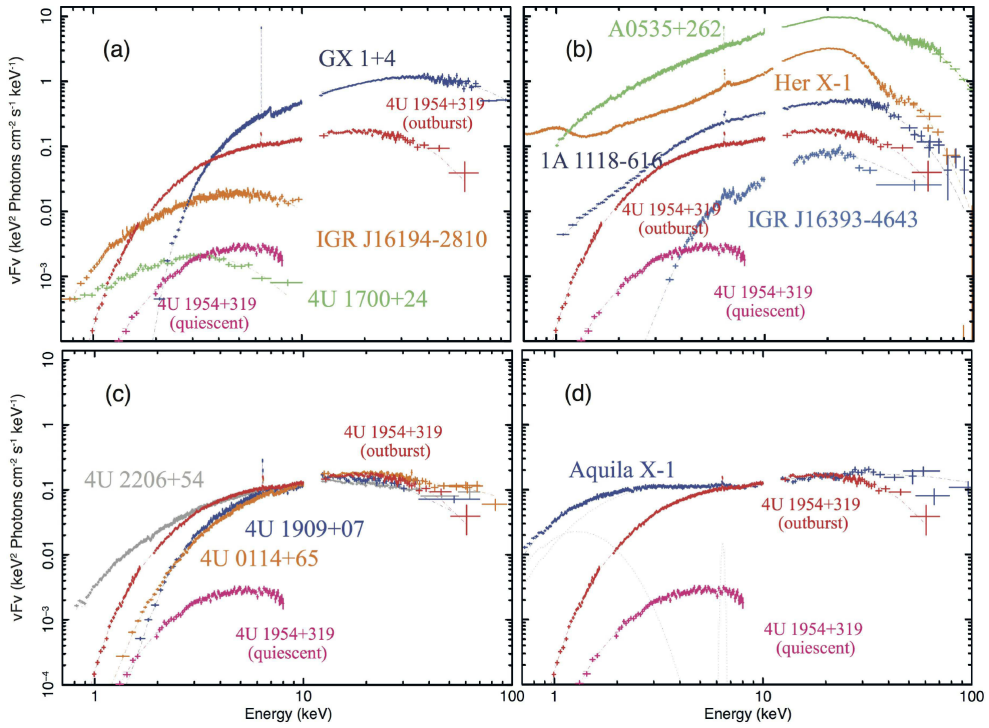

FIGURE 1.11: Various spectra of NS systems (Enoto et al., 2014). (a) SyXBs, (b) CRSF sources, (c) long period pulsars, and (d) Aquila X-1 in low/hard state.

A high-energy component

Some HMXBs have a little bit complex shape consists of high and low energy components in their low luminous states as shown in figure 1.12(Tsygankov et al., 2019a; Tsygankov et al., 2019b). The shape of the low energy component $\lesssim$ 20 keV is reminiscent of the typical HMXBs, while the additional component appears in the high energy region $\sim$ 50 keV. The emission mechanism of this high-energy component is still unknown. Tsygankov et al., 2019a explained the origin of the high-energy component for A 0535+262 by the recombination of the electrons in the heated layer of the NS atmosphere.

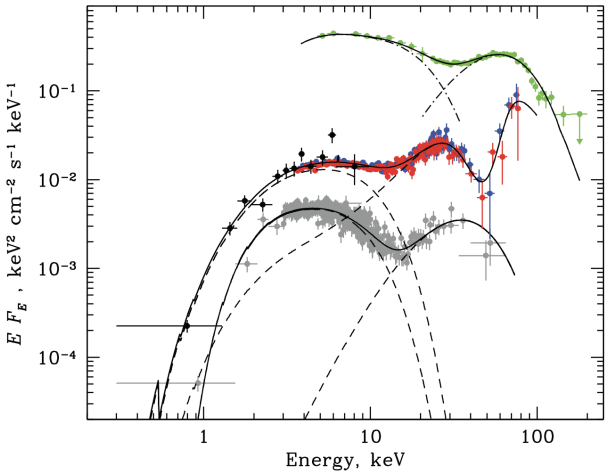

FIGURE 1.12: An example of the high-energy component. All spectra are taken from a HMXB, A0535+262, and the high-energy component appeared only in the low luminous state. This figure is adapted from (Tsygankov et al., 2019a).

A positive correlation of MF and cutoff energy

A positive correlation between the MF (CRSF) and the cutoff energy has also been suggested (figure 1.13). The origin of this observational result is not studied well. One of the keys to understand this phenomenon is a cyclotron cooling. In the strong MF, the transverse motion of the electrons is extremely restricted, and the cyclotron cooling does not work efficiently. As a result, the high energy emission will appear on their spectrum (Mihara, 1995).

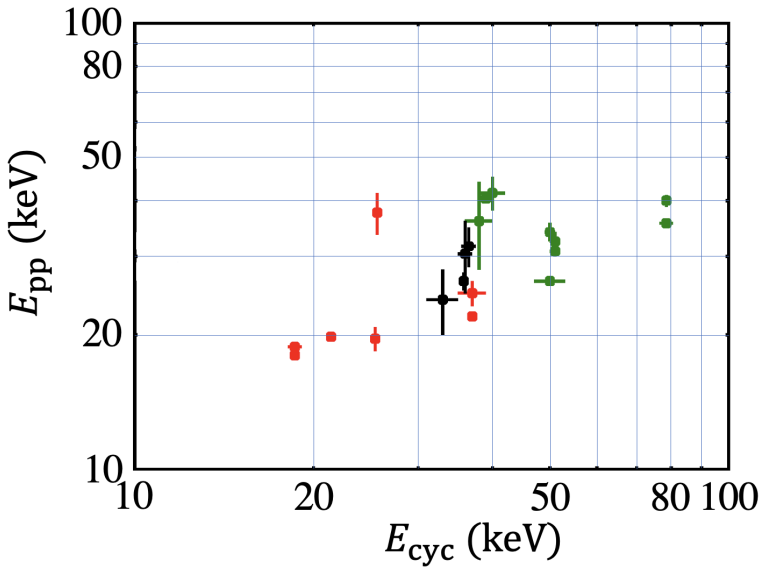

FIGURE 1.13: The empirical relation between the energy of positive power-law peak and cyclotron resonance. This figure is adapted from (Sasano, 2014) which originated by Makishima et al., 1999.

"harder when brighter" trend

An interesting spectral behavior, the "harder when brighter" trend, is observed in some HMXBs when they are < 0.1 times the Eddington luminosity (Ballhausen,

Ralf et al., 2017; Reig, P. and Nespoli, E., 2013) as shown in figure 1.14. The power exponent of the spectrum becomes harder as the luminosity increase. Ballhausen, Ralf et al., 2017 explained this behavior by an increase of the inverse-Compton scattering probability as an increase of accretion rate.

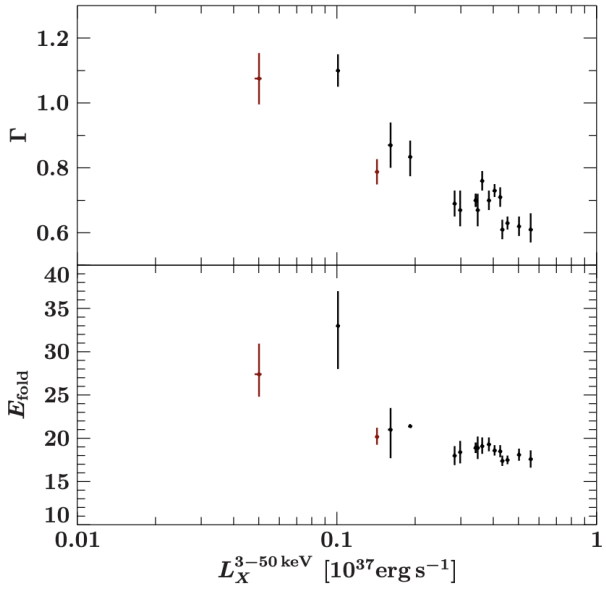

FIGURE 1.14: The "harder when brighter" trend observed from A 0535+26. The lower panel is the relationship for the cutoff energy. This figure is adapted from (Ballhausen, Ralf et al., 2017)

Chapter 2

Scientific Motivation

In the previous chapter, we summarized the NS population by their spin periods, radiation (accretion) mechanisms, and surface MFs. Here, we described the missing pieces for understanding the diversity of NSs.

2.1 Enigma: Surface Magnetic Field Strength

The MF strength B on the NS surface is one of the most important parameters for understanding the accretion geometry and X-ray emission process. FIGURE 2.1 shows B distribution for some kind of NSs. This is equivalent to the B-axis projection of FIGURE 1.2.

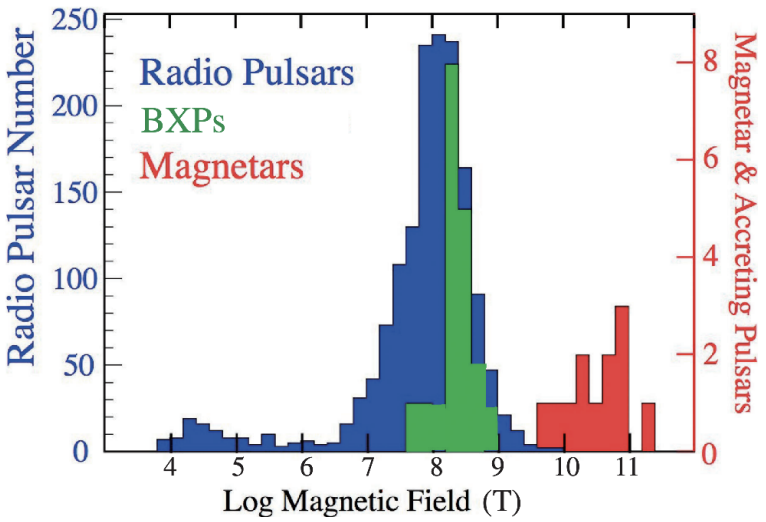

FIGURE 2.1: Histogram of NS surface MFs for some NS classifications.(Makishima, 2016)

There seem to be three peaks around 10^8, 10^{12}, and 10^{15} G (1 G $= 10^{-4}$ T). The origin of these three peaks cannot be explained by the evolution of NS and is not yet understood. Especially for the gap between 10^{12} G and 10^{15} G, we currently cannot distinguish whether the gap is caused by the selection effect due to the difficulty of detecting the CRSF or NSs nature. The accretion torque model will allow us to fill (or dig) this gap since it can apply for the MF of over 10^{12} G. According to the results on X Persei (Yatabe et al., 2018), such an accreting NS with a very strong B is expected to have a long spin period and a low luminosity because the large magnetosphere suppresses the accretion. There are no applications of GL79 for the wind-accreting NSs so far. NSs are born in a supernova with a MF of 10^{12} G and grow up with decreasing their MF. Magnetars are thoughts to be born and evolve lonely since all of

the magnetars are found as the isolated system. In other words, the magnetars were thought to be following the different evolution scheme with ordinary NSs. However, the highly magnetized NS, X-Per, was found in the binary system. Such objects, if plenty, would challenge the consensus that magnetars are found solely as isolated NSs. We are hence urged to search for similar X-ray sources.

2.2 Enigma 2: X-ray Emission Mechanism

The spectrum should be affected by the MF since X-ray is thought to be produced in the accretion column where the MF is dominant. Quantum mechanical effects also cannot be ignored in the highly magnetized NSs over $>10^{12}$ G. There are many interesting spectral behaviors and features that are possibly related to the surface MF as described in section 1.5. A detailed and systematic spectral analysis of a HMXB is required to reveal the origin of these features. However, we need to carefully choose a target since the low luminosity, caused by the propeller effect, is expected for a highly magnetized accreting system. To find the highly magnetized NS in the binary system, slow spin period and low luminosity are the most important requirements. It is also important that a presence of many observational data with various luminosity states.

2.3 High-Mass X-ray Binary: IGR J00370+6122

One of the best candidates of the highly magnetized NS in binary system is IGR J00370+6122.

IGR J00370+6122 is a high-mass X-ray binary discovered by the INTEGRAL satellite in 2003 (Hartog et al., 2004). The distance was measured as $3.4^{+0.3}_{-0.2}$ kpc (Brown et al., 2018, Hainich et al., 2020). An average flux of the RXTE/ASM light curve was <1 mCrab and 3 mCrab ($\sim 10^{35}$ erg/s) during the quiescent and flare phases, respectively (Hartog et al., 2004). The 3-60 keV flare X-ray spectrum was modeled with an absorbed power-law emission (in 't Zand et al., 2007). The optical counterpart is BD+60 73, of which spectral type was reported as B1 Ib (Morgan, Code, and Whiteford, 1995), B0.5II-III (Reig et al., 2005), or BN0.7Ib (González-Galán et al., 2014). The circumstellar disk was not found (Reig et al., 2005). The orbital period and eccentricity were reported 15.6627±0.0042 and 0.56±0.07 (in 't Zand et al., 2007, Grunhut, Bolton, and McSwain, 2014) or 15.6610±0.0017 and $0.48^{+0.02}_{-0.03}$ (González-Galán et al., 2014).

The compact object is a probable pulsar with a period of 346±6 s, since an RXTE/PCA light curve showed a 1-h flaring activity with an oscillating signal repeating 7 times (in 't Zand et al., 2007). The light curve which reported in in 't Zand et al., 2007 is shown in FIGURE 2.2, and the resultant chi-square periodogram is also shown in FIGURE 2.3. We can confirm the $\sim$ 346 s-like periodicity in the RXTE/PCA light curve only in the brighter term in the observation. The resultant periodogram has three large peaks around 346 s, 550 s, and 700 s. in 't Zand et al., 2007 argues that the period of 346 is the most coherent in terms of the relative width of the peak in FIGURE 2.3.

It is only this observation that the possible pulsation has been reported. Hainich et al., 2020 analyzed one Swift/XRT observation in a quiescent state and reported that the X-ray luminosity reached as faint as $\sim 10^{32}$ erg s^{-1}. These behaviors resemble that of the behavior of Supergiant Fast X-ray Transients (SFXTs), which consist of a highly magnetized NS (Bozzo, Falanga, and Stella, 2008). Since the measured spin

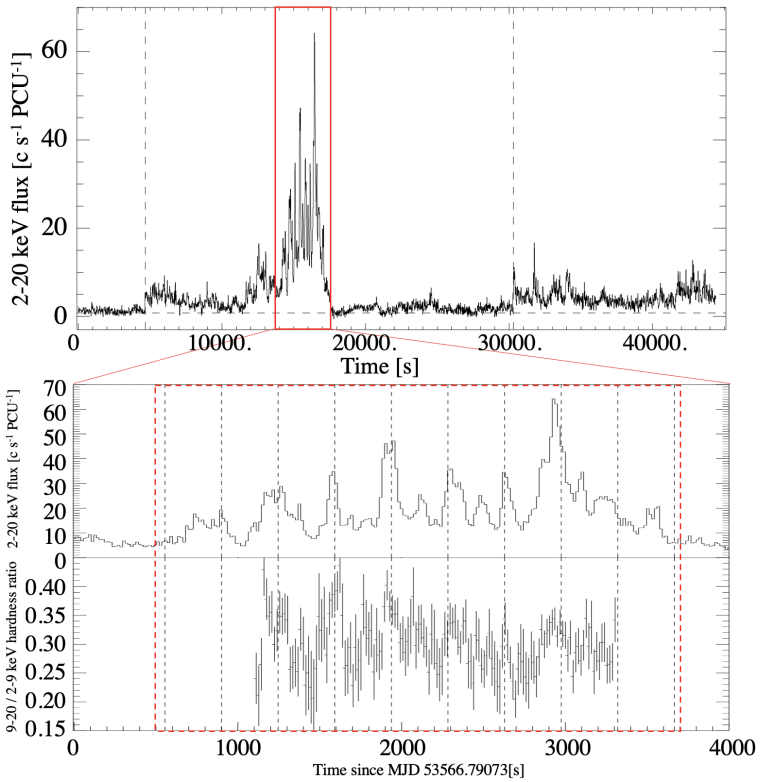

FIGURE 2.2: Background-subtracted light curve of IGR J00370+6122 with the RXTE/PCA in 2-20 keV. (in 't Zand et al., 2007)

.

period was slow and the X-ray luminosity was faint, the NS was estimated to have the strong MF of 10^{15} G corresponding to a magnetar and/or very inefficient accretion (Grunhut, Bolton, and McSwain, 2014). The optical orbital modulation was not able to rule out the possibility of a black hole (Grunhut, Bolton, and McSwain, 2014, González-Galán et al., 2014).

In the present paper, we analyze the following X-ray data of IGR J00370+6122. First, we reanalyze the 15-year Swift/BAT monitor data to obtain the accurate orbital position for all data in this paper. Second, we search the pulsation in a 23-ks XMM-Newton observation during the flare phase for investigating whether the companion is a NS or black hole. Finally, we perform orbital-phase dependent spectral analyzes of XMM-Newton, Suzaku, Swift/XRT, RXTE, and INTEGRAL to probe into the identity of the companion star.

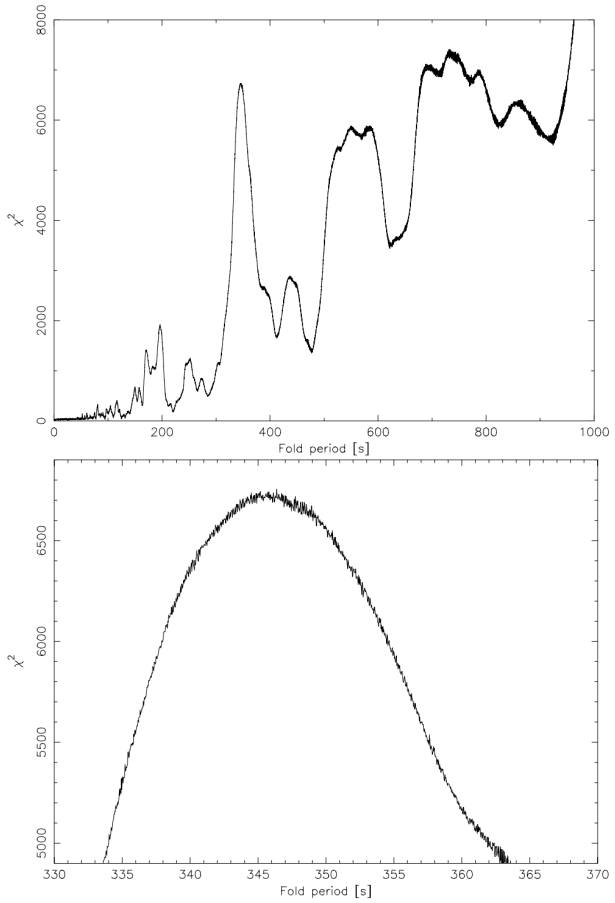

FIGURE 2.3: Chi-square periodogram for the light curve in FIGURE 2.2 with the search resolution of 1/32. The bottom figure is an expanded periodogram in a range of 330–370 s.

.

Chapter 3

Instruments

We analyzed two kinds of observational data of IGR J00370+6122. One is pointing data executed by XMM-Newton/EPIC, Suzaku/XIS, Swift/XRT, and RXTE/PCA, while the other is monitoring data by Swift/BAT, RXTE/ASM, and INTEGRAL/ISGRI. For the pointing dataset, we performed timing (light-curve) and energy spectral analyzes. In this section, let me explain these satellites and instruments.

3.1 XMM-Newton

XMM-Newton is a satellite that was developed/launched by the European Space Agency (ESA) in 1999 and is still in operation (as of Feb. 2021). The satellite is orbiting far from the Earth with an ellipse of 115000 km at apogee by 6000 km at perigee. This satellite can be characterized by its large effective area in the X-ray band (0.1–15 keV) which is supported by three X-ray telescopes. These telescopes consist of 58 Wolter I grazing-incidence mirrors which were manufactured by replica method. The diameter of the largest mirror is 70 cm, and the focal length is 7.5 m. Two front-illuminated CCDs (MOS1, MOS2) and one back-illuminated CCD (PM) are located in the focal planes for these telescopes. Reflection Grating Spectrometers (RGSs), which consist of Reflection Grating Assemblies (RGAs) and RGS Focal Cameras (RFCs), are inserted in two of three telescopes and collect the soft X-ray photons in the 0.35–2.5 keV range. The roughly 40% of the incident photons are diffracted by RGAs and intercepted by RGSs, while the 44% are passing through RGAs and observed by the MOS detectors. The rest of 14% of the incident photons are absorbed by RGAs. An optical monitor (OM) also enables us to observe in the UV and the blue region of the optical spectrum with the limiting magnitude of B=24 (unfiltered).

The background level of XMM-Newton is relatively high since it is orbiting outside of the Earth's magnetosphere while it enables us to observe objects without being eclipsed by the Earth.

In the present study, we mainly used MOS1, MOS2, and PN (collectively called EPIC) for spectral and pulse timing analysis.

The effective area of the EPIC detectors is shown in FIGURE 3.1. The total effective area for three EPIC detectors is the largest for the present X-ray satellite mission. The effective area is mainly determined by the X-ray telescope.

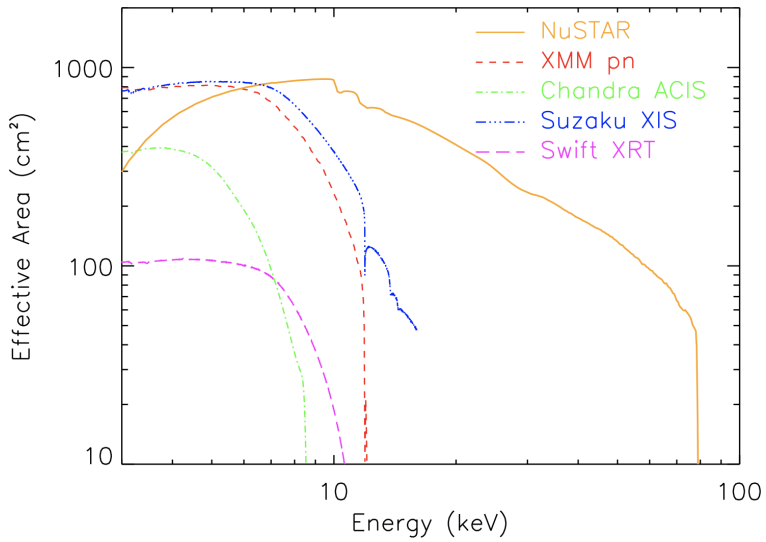

FIGURE 3.1: Comparison of the effective areas for some X-ray satellite missions (Harrison et al., 2013)

Depending on the magnitude of the observed object and the required time resolution, EPIC has the following observation modes.

- Full frame / Extended full frame (PN only)
- Large window / Small window
- Timing / Burst (PN only)

In the present analysis, we used the small window and full window modes. The small window mode was employed for the timing and spectral analysis since it they have enough timing resolutions of 0.3 s for MOS and 5.7 ms for PN to trace a second order of the time fluctuations of HMXB. Data taken in the full window mode was used only for a spectral analysis since it has not enough timing resolution (2.6 s) but detected the quiescent phase of the target in its edge of the FoV.

3.2 Suzaku

Suzaku is a Japanese X-ray satellite that was developed as a fifth in the ASTRO-series mission. This satellite was launched into quasi-circular orbit, in which an altitude of ∼570 km and an inclination angle of 30 degrees, in 2005. The satellite stopped observations and operations due to a trouble in its batteries in 2005. A lot of scientific achievements and publications are produced from Suzaku. All of the observed data are archived, and anyone can access these data via Data ARchives and Transmission System (DARTS). The background level of the detectors onboard Suzaku is extremely low since it was orbiting inside of the Earth's magnetosphere. On the other hand, a disadvantage of the low-earth orbit (LEO) is also appeared as the observational duty cycle of ∼ 45% due to the South Atlantic Anomaly (SAA) and the obstruction of the target by the Earth. Suzaku has five Wolter-I X-ray telescopes which can be divided into two types by the number of mirror layers, i. e. XRT-I and XRT-S. The diameters of both XRT-I and XRT-S are 40 cm. The number of mirror layers and the focal lengths are 175 and 5.75 m for XRT-I, and 168 and 4.5 m for XRT-S, respectively. One X-ray spectrometer (XRS) is placed on the focal plane of XRT-S, and four CCDs (X-ray Imaging Spectrometers; XISs) for XRT-I to detect soft X-ray

(0.2–12 keV) photons. XIS1 is back-illuminated CCD, while the others are front-illuminated CCD. For the high energy (10–600 keV) band, a hard X-ray detector (HXD) is mounted beside XISs. A schematic view of the Suzaku satellite is shown in FIGURE 3.2.

In this study, we mainly used the XIS detectors for the spectral analyzes by making use of its low background and high sensitivity. The effective area of XIS is drawn in FIGURE 3.1.

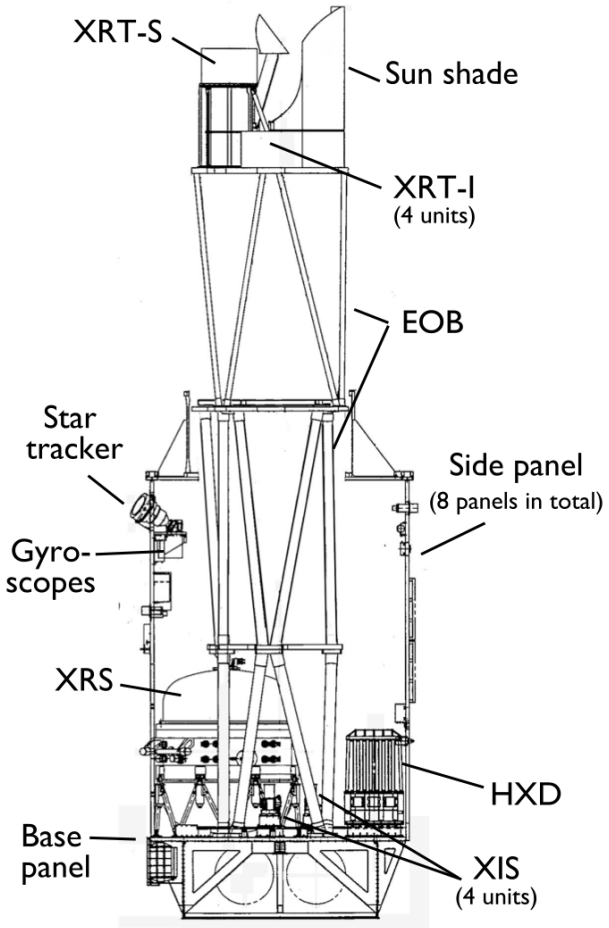

FIGURE 3.2: A cross-section of the Suzaku satellite(Mitsuda et al., 2007)

3.3 Swift

Swift was developed as one of the medium-class explorers by NASA with the international collaboration of the United States, United Kingdom, and Italy. The satellite was launched in 2004 into LEO, in which an altitude of 600 km and an inclination of 20.56°, to identify the Gamma-ray bursts. The satellite can observe Gamma-ray bursts in a wide energy range from optical to Gamma-ray thanks to three detectors. Transient events are firstly detected by a burst alert telescope (BAT) and automatically calculate the burst location by itself on-orbit. After determined the burst position, the satellite automatically starts the follow-up observation by X-ray telescope (XRT) and UltraViolet and Optical Telescope (UVOT).

The BAT detector is constructed by a CdZnTe Semiconductor detector array and a 2-dimensional coded aperture mask. The Gamma-ray spectrum and images are

monitored by BAT in an energy range of 15–150 keV. It is difficult to form an image for Gamma-ray with the energy of over several ten keV. However, BAT pulls off this difficulty by using its coded mask. A part of incident photons is absorbed by the coded mask, while the other photons pass through the apertures of the mask. Therefore, a photon pattern, which depends on the incident angles of the Gamma-ray photons, were appeared on a focal plane. Images are reconstructed by analyzing this photon pattern. Processed light curves and spectra obtained by BAT are archived on its website.

The Swift/XRT is sensitive in the energy of 0.3–10 keV with an energy resolution of $\sim$ 140 eV (at 6 keV). This telescope is a spare of a Spectrum X-Gamma mission, and a CCD placed on the focal plane is the equivalent of the XMM-Newton/EPIC. The angular resolution is $2'' - 5''$ with the field-of-view of 23.6×23.6 arcmin.

The XRT has three readout modes, i.e. Photodiode (PD) mode ($\sim$ 0.14ms)、Windowed Timing (WT) mode (1.8ms)、Photon-counting (PC) mode (2.5s). The PD mode has the best timing resolution of 0.14 ms with no spatial information; however, this mode is now unusable because of a micrometeorite attack. The window mode (WT) is another fast timing ($\sim$ 1.8 ms) mode with a 1D image. The photon-counting mode (PC) can take 2D imaging and spectroscopy with a time resolution of 2.5 s. An additional mode that is specified to localize transients like gamma-ray burst is also equipped to XRT. This mode only outputs the location information of transients. The data we used in this study were all taken in PC mode.

3.4 RXTE

The Rossi X-ray Timing Explorer (RXTE; Bradt, H. V., Rothschild, R. E., and Swank, J. H., 1993) was developed mainly focused on observing compact objects, i.e. black-holes, NSs and transients, with its high time resolution in high energy band. This satellite was developed and launched by NASA in 1995 into LEO and operated until 2012. This satellite had three non-imaging detectors, one is Proportional Counter Array (PCA), another is High Energy X-ray Timing Experiment (HEXTE) and the other is All-Sky Monitor (ASM). PCA is a proportional counter-based detector consists of five detector cells (PCU0 to PCU4). Each unit is filled with Xe gas. The Xe layers are separated into three layers in horizontal and two parts in vertical (see FIGURE 3.3) for each unit. A total photon-collection area is 6500 cm^3 in the energy range of 2–60 keV. The incident photons to PCA are collimated with a FWHM of 1° by a passive collimator consists of narrow hexagonal tubes for each unit. Some non-X-ray backgrounds are blocked by these collimators. The obtained data were processed by Experiment Data System (EDS) onboard the RXTE satellite. The reduced event data for the PCA detector consists of two modes, i.e. Standard1 and Standard2. The Standard1 data has a good time resolution of 1/8 s with a sacrifice of an energy resolution, while Standard2 has a time resolution of 8 s with a spectral capability.

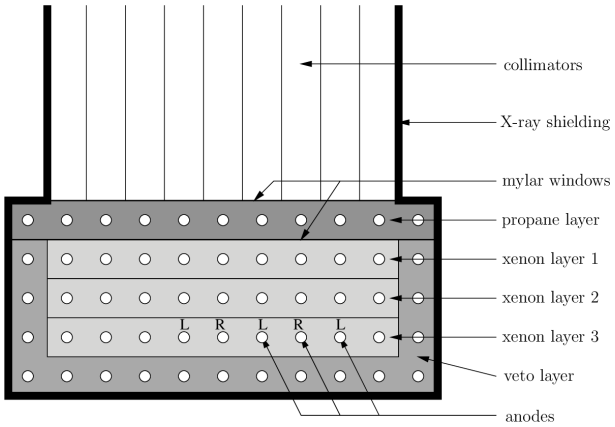

FIGURE 3.3: A schematic drawing of the RXTE/PCA unit.(Wei, 2006)

HEXTE consists of 2 clusters of detectors. Each detector consists of four phoswich-type scintillation detectors for high energy (15–250 keV) observations. The NaI crystals are employed as the main absorber, while the CsI crystals are as an active anticoincidence collimator. The typical energy resolution is 18% (at 60 keV) with the effective areas of 1200 cm^2, 1100 cm^2, and 300 cm^2 for 50 keV, 100 keV, and 200 keV, respectively. The HEXTE detectors are coaligned with the PCA detectors for observing the same object with a wide energy range.

ASM was monitoring all-sky with the effective field of view of $\Omega = 2.97 \times 10^{-4}$ sr(Revnivtsev, M. et al., 2003), in contrast to the pointing observation of PCA and HEXTE. ASM had three Scanning Shadow Cameras (SSCs) which were equipped with Xe-filled proportional counters with one-dimensional position sensitivity. Each SSCs have a collimator with $6° \times 90°$ mounded on a rotating drive assembly and allow us to observe the 80% of the sky every 90 minutes with the spatial resolution of $3' \times 15'$. An energy range of ASM is 2–10 keV and a sensitivity reach $\sim$ 20 mCrab.

3.5 INTEGRAL

INTEGRAL was developed by ESA with the corporation of Russia, Czech, and Poland. The satellite was injected into a highly elliptical orbit with an inclination of 51.6°, an altitude of 153,000 km at apogee, and 9,000 km at perigee in 2002. Therefore, INTEGRAL is orbiting well outside of Earth's radiation belts and can avoid the background radiation consists of high-energy particles. The satellite mainly focusing on the hard X-ray and Gamma-ray (18 keV–8 MeV) observation of cosmic-ray. INTEGRAL has three X-ray and Gamma-ray detectors and one optical monitor called optical camera on-board INTEGRAL (OMC). These three detectors, Imager on Board the INTEGRAL Satellite (IBIS), SPectrometer for INTEGRAL (SPI), and Joint European X-Ray Monitor (JEM-X), have a localization capability with their coded masks.

IBIS consists of two detector planes for the different energy range, i. e INTEGRAL Soft Gamma-Ray Imager (ISGRI) for 15–500 keV and Pixellated Imaging Caesium Iodide Telescope (PICsIT) for 175 keV–10 MeV. ISGRI is located a top layer and PICsIT is a bottom layer of the IBIS detector configuration. ISGRI is a CdTe-based semiconductor detector consists of eight modules of 64×32 CdTe pixels, while PICsIT is a scintillation-based detector with CsI crystals. The total field-of-view is $29.1° \times 29.4°$. SPI is a spectrometer with a wide energy range of 18 keV–8 MeV and

an energy resolution of 2.2 keV (at 1.33 MeV). The detector is comprised of an array of 19 hexagonal Germanium detectors. All the detector units are operated at a low temperature of 85 K by a Stirling cooler system. IBIS and SPI have the capability of measuring polarization. However, an evaluation of systematic uncertainty is not so easy since they are not specialized for polarization measurement. JEM-X is covering an energy range of 3–35 keV with some microstrip gas chambers filled with Xe and CH_4. This detector has the role of the detection and identification of X-ray sources by using its good angular resolution of ~ 30 arcsec thanks to the coded mask located on the top part of the detector.

In general, a coded mask-based imager has a low signal-to-noise ratio (S/N) compared to the telescope-based imager since a part of the incident photons are absorbed by the coded mask, while the background is proportional to the collection area of the detector. The sensitivity of IBIS, SPI, and JEM-X is 1 mCrab (100 keV), 50 mCrab (100 keV), and 1 mCrab (30 keV), respectively. The INTEGRAL/IBIS is still holding one of the largest effective areas over 20 keV.

Chapter 4

Observation and data reduction

The present work begins with an analysis of the orbital intensity modulation of IGR J00370+6122, utilizing the Swift/BAT data covering 15 yr from 2005 to 2019. Then, to derive orbital variations of the X-ray luminosity, we analyze the data from 34 pointing observations; as summarized in table 4.1, these consist of two observations made with XMM-Newton of which one caught a flaring state, one with the Suzaku/XIS in which the source was quiescent, and the remaining 31 from the Swift/XRT. Of these, the flaring-state data set with XMM-Newton is employed also in a search for pulsed signals. In addition, detailed spectral evaluations are conducted using the same XMM-Newton data, those from Suzaku, and the 5 brightest of the Swift/XRT data sets. Finally, to expand the upper energy boundary to $\sim$ 80 keV, we incorporate an RXTE/PCA spectrum taken in 2005 (in 't Zand et al., 2007), and a 10-yr average spectrum of IGR J00370+6122 taken with the INTEGRAL/ISGRI (Walter et al., 2011). All spectral analyzes are executed with xspec (version 12.10.1).

4.1 XMM-Newton

IGR J00370+6122 was observed twice by XMM-Newton. We reduced these data using the Science Analysis System (SAS) version 18.0, and generated the cleaned event lists from EPIC PN and EPIC MOS, utilizing the `emchain` and `epchain` tasks, respectively. In the first observation, the three EPIC detectors (MOS1, MOS2, and PN) were all operated in the Small Window mode. The on-source events with the three EPIC detectors, covering a 0.1–15 keV range, were extracted from a circular region of $35''.0$ radius centred on IGR J00370+6122. Background events of MOS1 and PN were derived from a source-free circular region on the same CCD, with a radius $20''.0$ and $35''.0$, respectively. Those of MOS2 were taken from an annular region with the inner and outer radii of $40''.0$ and $47''.5$, respectively. In the second observation, the source was observed only in the field-of-view of MOS2 with the Prime Full Window mode. Source and background photons were collected from a circular region with a radius of $25''.0$ and an annular region with inner and outer radii of $60''.0$ and $70''.0$, respectively. All of the source and background regions are drawn on the respective image in figure 4.1. To produce spectra and light curves, we use `evselect`, whereas response matrix files (RMFs) and ancillary response files (ARFs) are generated using `rmfgen` and `arfgen`, respectively. The pulse search is carried out using the XRONOS software package, distributed by High Energy Astrophysics Science Archive Research Center (HEASARC), For that purpose, we applied the barycentric corrections to all the photons, by `barycen` in the SAS software.

In the first observation, made in 2008 for a net exposure of 23 ks, the source exhibited a strong flaring activity around a mean luminosity of $\sim 1 \times 10^{35}$ erg s^{-1}. In the second XMM-Newton observation conducted in 2016 for a net exposure of 11 ks, the source luminosity was much lower, $\sim 1 \times 10^{32}$ erg s^{-1}. Figure 4.2 shows

TABLE 4.1: The data sets of IGR J00370+6122 utilized in the present paper.

ObsID	Date (MJD)	Orbital phase*		
		(1)	(2)	(3)
(RXTE)				
91061010101	53566.78648-53566.84870	0.217-0.221	0.120-0.124	0.144-0.148
XMM-Newton				
0501450101	54505.86816-54506.13731	0.173-0.190	0.083-0.101	0.093-0.110
0742800201	57411.18597-57411.32056	0.666-0.674	0.596-0.605	0.560-0.568
(Suzaku)				
402064010	54273.51784-54274.21653	0.338-0.383	0.247-0.292	0.260-0.305
(Swift)				
00032620001	56319.00870-56319.27982	0.935-0.952	0.858-0.875	0.838-0.856
00032620002	56327.70678-56327.92077	0.490-0.504	0.413-0.427	0.393-0.407
00032620003	56331.71219-56331.85617	0.746-0.755	0.669-0.678	0.649-0.658
00032620004	56335.57914-56335.66229	0.993-0.998	0.916-0.921	0.896-0.901
00032620005	56339.11291-56339.19714	0.218-0.224	0.141-0.147	0.122-0.127
00032620006	56343.18709-56344.00067	0.478-0.530	0.402-0.454	0.382-0.434
00032620007	56347.25626-56347.33956	0.738-0.744	0.661-0.667	0.641-0.647
00032620008	56351.06961-56351.14633	0.982-0.987	0.905-0.910	0.885-0.890
00032620009	56355.40697-56355.49373	0.259-0.264	0.182-0.187	0.162-0.167
00032620010	56359.47223-56359.75754	0.518-0.536	0.441-0.460	0.421-0.439
00032620011	56363.41796-56363.49504	0.770-0.775	0.693-0.698	0.673-0.678
00032620012	56367.42019-56367.96859	0.026-0.061	0.949-0.984	0.929-0.964
00032620013	56371.09796-56371.37501	0.260-0.278	0.184-0.201	0.163-0.181
00032620014	56379.06295-56379.60814	0.769-0.804	0.692-0.727	0.672-0.707
00032620015	56383.06571-56383.95063	0.025-0.081	0.948-0.004	0.927-0.984
00032620016	56387.40246-56387.95629	0.301-0.337	0.225-0.260	0.204-0.240
00032620017	56391.20790-56391.28544	0.544-0.549	0.468-0.473	0.447-0.452
00032620018	56395.60485-56395.68474	0.825-0.830	0.749-0.754	0.728-0.733
00032620019	56399.80960-56399.89170	0.094-0.099	0.017-0.022	0.996-0.002
00032620020	56403.02594-56403.22481	0.299-0.312	0.222-0.235	0.202-0.214
00032620021	56407.49091-56407.57205	0.584-0.589	0.508-0.513	0.487-0.492
00032620022	56411.36986-56411.56739	0.832-0.844	0.755-0.768	0.734-0.747
00032620023	56416.11359-56416.24773	0.135-0.143	0.058-0.067	0.037-0.046
00032620024	56420.57812-56420.90884	0.420-0.441	0.343-0.364	0.322-0.343
00032620025	57023.68172-57023.75550	0.925-0.930	0.853-0.858	0.822-0.827
00032620026	57024.47586-57024.94858	0.976-0.006	0.904-0.934	0.873-0.903
00032620027	57025.73281-57025.81511	0.056-0.062	0.984-0.989	0.953-0.959
00032620028	57026.67560-57026.74499	0.116-0.121	0.044-0.049	0.014-0.018
00032620029	57027.66365-57027.74351	0.180-0.185	0.107-0.112	0.077-0.082
00032620030	57028.06750-57028.94092	0.205-0.261	0.133-0.189	0.102-0.158
00032620031	57029.19426-57029.94580	0.277-0.325	0.205-0.253	0.174-0.222

Orbital phases are calculated based on the ephemeris obtained by (1) Grunhut, Bolton, and McSwain, 2014, (2) González-Galán et al., 2014, and (3) in the present work.

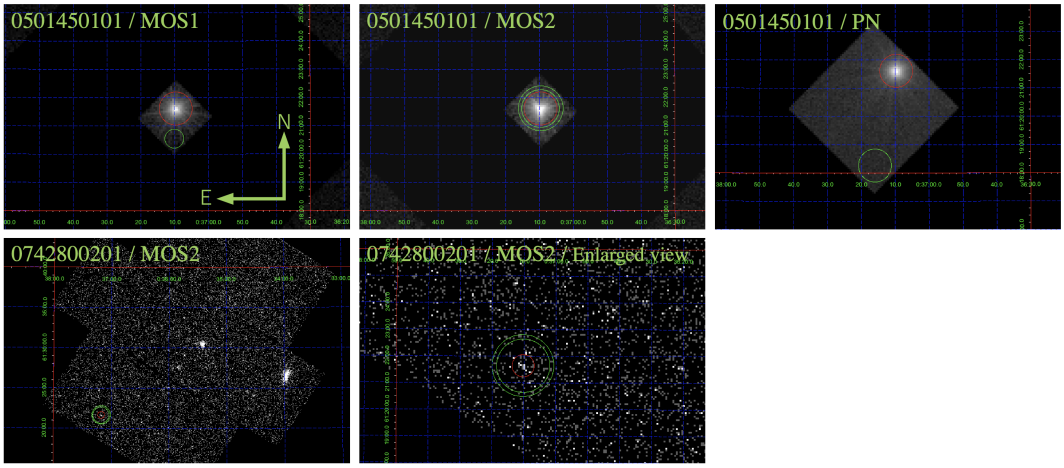

FIGURE 4.1: The image that constructed from the XMM-Newton observations. The source and background regions are shown in the red and green circle (or annulus), respectively. In the figure, the upper direction is north and, the left direction is east. The top three panels are the images for the first observation. The bottom left panel is the full image of the MOS2 of the second observation. The enlarged view of the source region is also shown in the bottom right panel.

an EPIC/PN light curve from the 1st observation, in the 0.1–15 keV energy range (without energy selection in the events). In the first half of the observation, we observe high count rates and strong intensity variations. The MOS1 and MOS2 data acquired in this observation are incorporated later in the spectral analyzes.

4.2 Suzaku/XIS

The archival Suzaku data of IGR J00370+6122, in the 0.2–12 keV range, were acquired in 2007 (MJD 54274). Of the four XIS cameras, we utilize the data from XIS0, XIS1, and XIS3, which were operated with 1/4 window mode at that time. The HXD data are not employed, because IGR J00370+6122 was not detected by the HXD. We processed and screened the XIS data with `aepipeline` 1.1.0. and extracted source and background event with `xselect`. The source events were accumulated over a

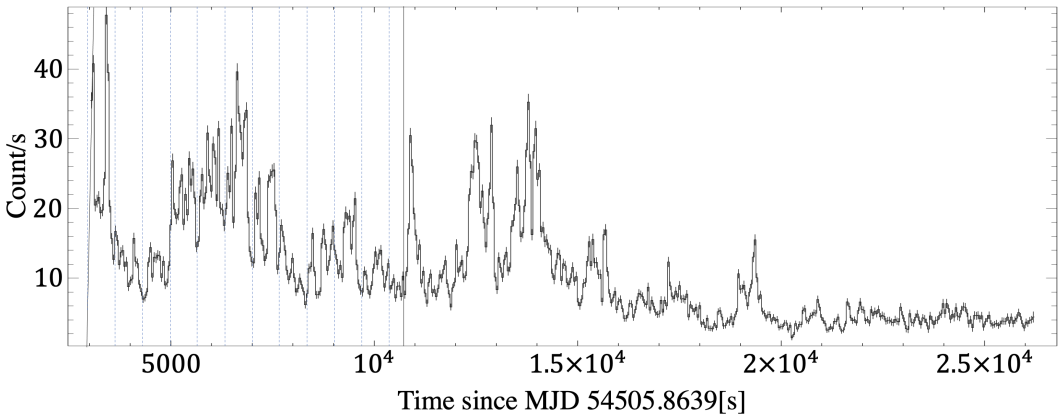

FIGURE 4.2: Background subtracted 0.1–15 keV light curve of IGR J00370+6122, acquired in the second XMM-Newton observation with EPIC/PN. The vertical lines indicate the 674 s periodicity.

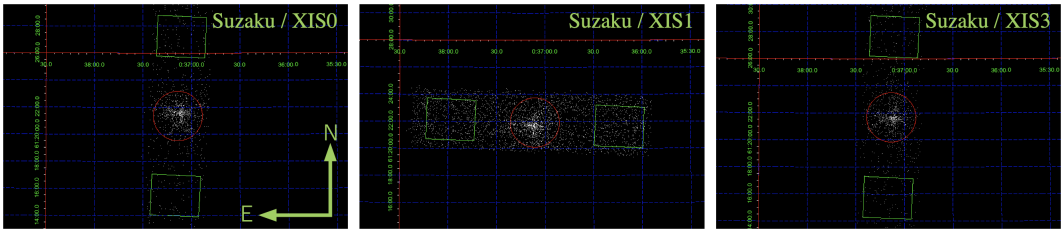

FIGURE 4.3: The image of the source and background regions for XIS0, XIS1, and XIS3 (from left to right). The red circles and green rectangles are the source and background region, respectively.

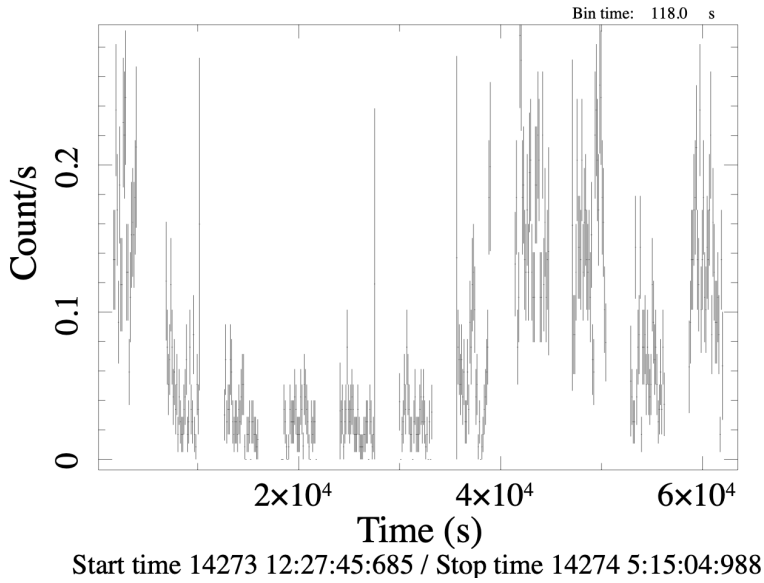

FIGURE 4.4: The suzaku/XIS0 light-curve which was extracted from the source region without subtracting the background.

circular region with 110″ radius around the source position. The background events were derived from two rectangular regions, both having a size of 180″ × 216″ and located at 0°.1 off the source. The images taken by XIS0, XIS1, and XIS3 are shown in figure 4.3 with the source and background regions. The RMFs and ARFs were generated using `xisrmfgen` and `xisarfgen` in HEASoft, respectively. A slight flux changes were observed for the light curve taken in this observation (figure 4.4).

4.3 Swift/BAT and Swift/XRT

To improve the orbital ephemeris of IGR J00370+6122, we use its 15–50 keV Swift/BAT daily light curve from 2005 February to 2019 November, provided by the Swift/BAT Hard X-ray Transient Monitor project (Krimm et al., 2013).

IGR J00370+6122 was observed also with the Swift/XRT, 24 times during ∼ 100 days in 2013 (MJD 56319-56420), and 7 days in 2015 (MJD 57023-57029). These PC-mode data sets, 31 altogether, are also analyzed in the present work. We processed each data set, consisting of 0.2–10.0 keV photons, using `xrtpipeline`. and produced the spectra and light curves using `xrtproducts`. All of the images taken by Swift/XRT are shown in figure 4.5. The on-source events were extracted from a circle of 47” radius, and the background events from an annulus with the inner and outer radii of 94″ and 141″, respectively. A light curve was constructed by using these 31

observations and indicates the roughly 15.7 days periodicity as shown in figure 4.6. Note that the original Swift/BAT light curve downloaded from the web page (Krimm et al., 2013) had the fits header keyword of TIMEPIXR=0.5, meaning that the TIME value corresponds to the middle of the bin. We modified it from 0.5 to 0, so that the TIME value becomes the beginning of the bin (private communication with the Swift/BAT team at NASA/GSFC).

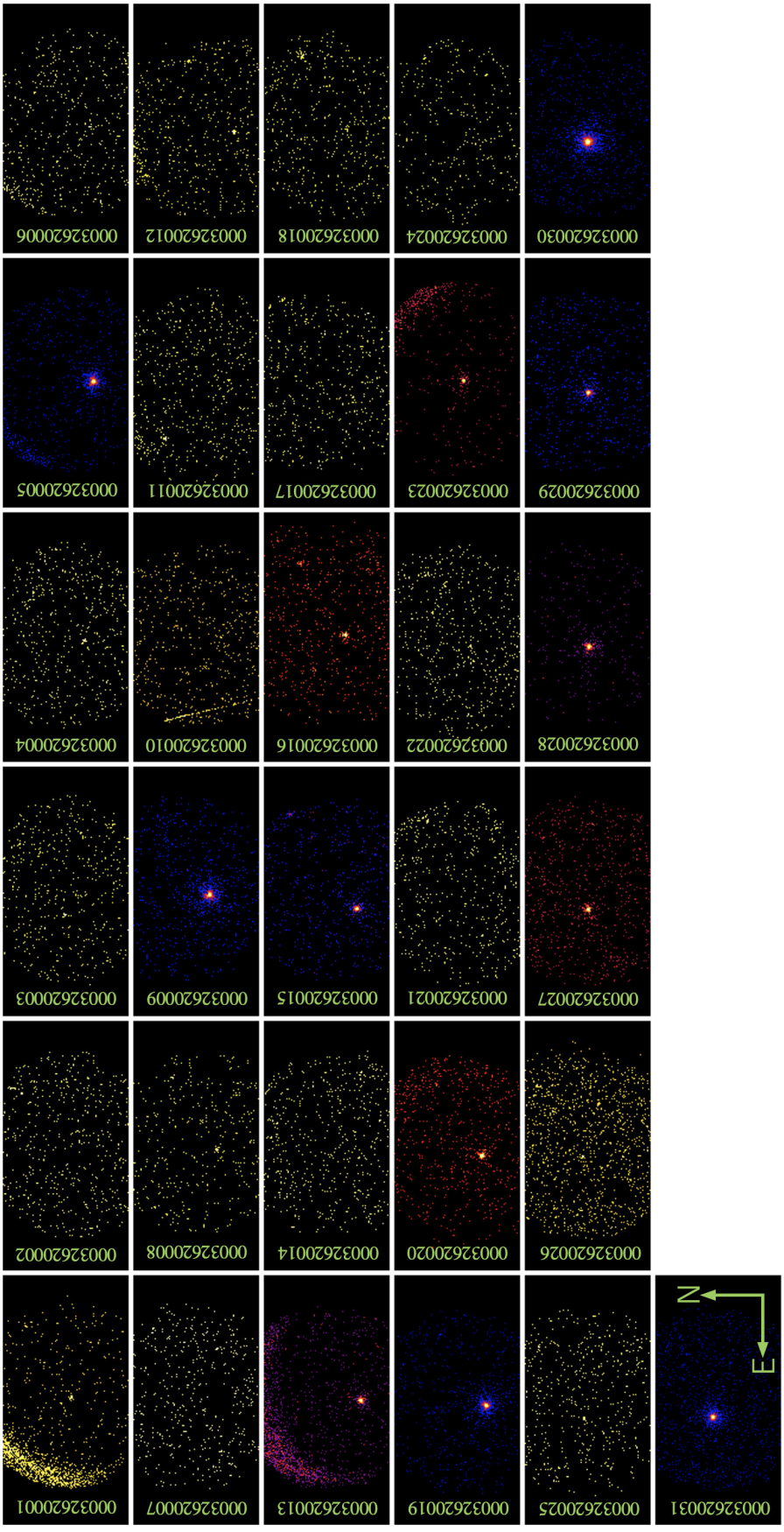

FIGURE 4.5: The images that constructed from all of the Swift/XRT observations.

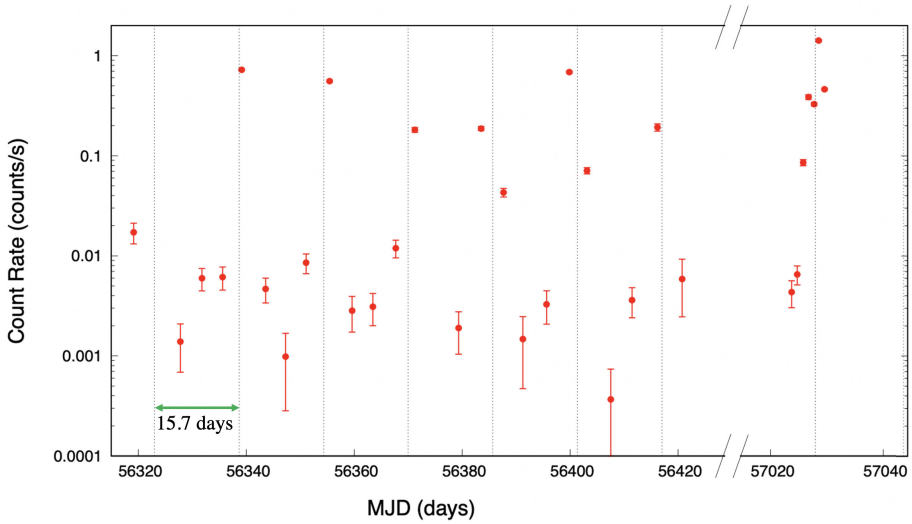

FIGURE 4.6: Light curve constructed from all Swift/XRT observations. The count rate for each data point is extracted from the source region without subtracting the background rate. The horizontal dashed lines indicate the 15.7 days periodicity.

4.4 The other data sets

The RXTE/PCA archival data, in which in 't Zand et al., 2007 detected the 346-s pulsation, were used to characterize the spectrum of IGR J00370+6122 in an intermediate energy range (7–30 keV). The background and response files are included in the same archive. We ignored <8 keV region to avoid Xenon L-edge feature.

The reduced INTEGRAL/ISGRI spectrum was downloaded from the site of High-Energy Astrophysics Virtually ENlightened Sky (HEAVENS), provided by the INTEGRAL Data Centre (ISDC). We selected 17.3–80.0 keV good-quality events that were acquired over 2003–2012 and in an orbital phase interval from -0.1 to 0.1. The background and response matrix were generated also by HEAVENS.

Chapter 5

Data Analysis and Results

5.1 Orbital intensity variations

As the first attempt of our data analysis, the 15-yr Swift/BAT light curve in 15–50 keV was analyzed for the expected 15.7 d orbital periodicity (in 't Zand et al., 2007; González-Galán et al., 2014), employing the standard epoch-folding method with chi-square evaluation. We used the `efsearch` software with 32 phase bins, and scanned the trial period from 12 d to 20 d with a step of 0.0007 d. The obtained periodogram is shown in figure 5.1. A strong peak seen around 15.66 d represents the orbital period, as reported in the previous works. By fitted this peak with a Gaussian, we determined the orbital period as

$$P_{\rm orb} = 15.6649 \pm 0.0014 \text{ d} \tag{5.1}$$

where the error refers to 90% confidence level. This $P_{\rm orb}$ is consistent with the previous measurements (in 't Zand et al., 2007; González-Galán et al., 2014), and has a better statistical accuracy, because we used a longer observation span.

Figure 5.2 is the 15–50 keV Swift/BAT light curve folded at $P_{\rm orb}$, where phase 0 is taken as the periastron time of

$$\text{MJD } 55084.018 \tag{5.2}$$

as determined by González-Galán et al., 2014. Thus, the source exhibits a strong orbital intensity variation, and has been detected with the Swift/BAT over a limited orbital phase of about -0.1 to 0.25. In addition, the intensity maximum is clearly delayed from the periastron by $\sim$ 0.05 orbital cycle, although the delay could be slightly smaller than the previously reported $0.1 - 0.2$ cycles (Grunhut, Bolton, and McSwain, 2014; González-Galán et al., 2014).

In table 1, we summarize the orbital phases of the individual observations analyzed in the present work, where the three columns for the orbital phase, (1) to (3), employ the three orbital solutions; Grunhut, Bolton, and McSwain, 2014, González-Galán et al., 2014, and the present work. Below, we utilize our own phase values, which are based on $P_{\rm orb}$ of equation (5.1) and the phase 0 (periastron) epoch of equation (5.2).

5.2 Search for pulsations

One of the most important objectives of the present study is to confirm that the compact object in IGR J00370+6122 is a magnetized NS powered via mass accretion. Evidently, the best way towards this goal is to detect a periodic source pulsation, at a period that is consistent with, or closely related to, the previously recorded 346-s periodicity. For this purpose, we choose the 1st observation with XMM-Newton,

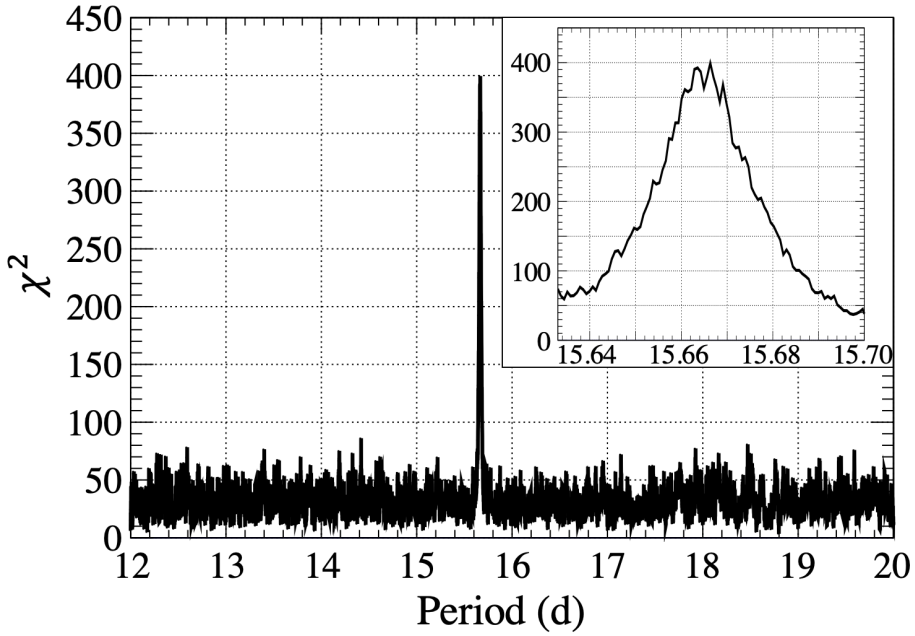

FIGURE 5.1: Periodgram of the 15-yr Swift/BAT data, revealing the orbital period. The inset shows an enlargement around the 15.7-d peak.

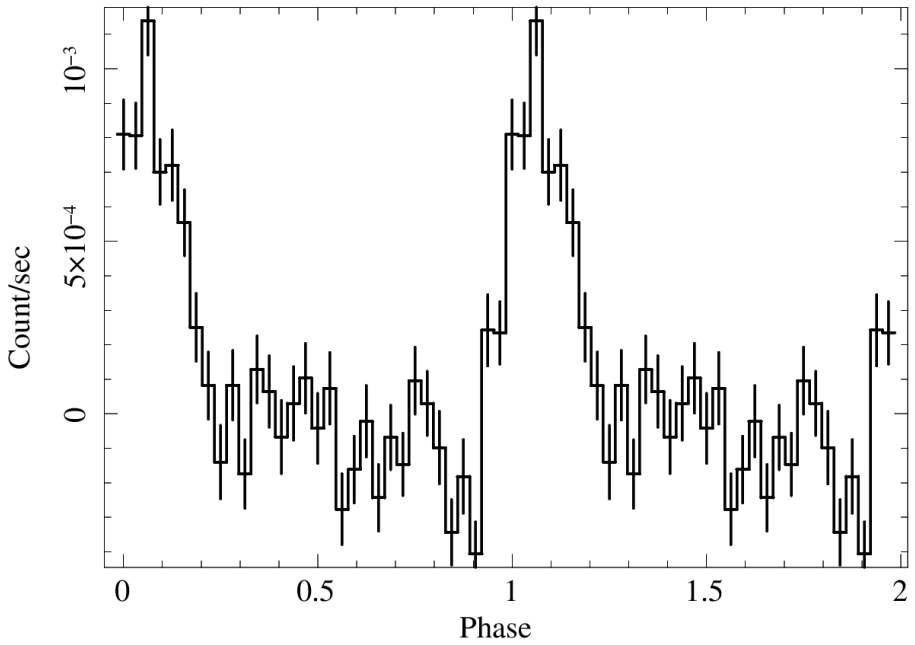

FIGURE 5.2: The Swift/BAT data, folded at $P_{\rm orb}$ of equation (5.1) and shown for two cycles. The epoch of phase zero is set as the periastron time given in González-Galán et al., 2014.

because the source was bright at that time, and exhibited multiple flares (figure 4.2) which are reminiscent of the case with in 't Zand et al., 2007.

5.2.1 Fourier power spectra

Using the background-subtracted 0.1–15.0 keV EPIC/PN light curve shown in figure 4.2 from this observation, and employing `powspec` with a time resolution of 1 s with which we generated the light curve, we calculated a Fourier power spectrum over a frequency range of $4 \times 10^{-5} - 0.5$ Hz. The result is presented in figure 5.3 in black, where the abscissa (i.e., the frequency) is shown in a logarithmic scale to better reveal the low-frequency region. The power is normalized so as to become 2.0 when the light curve is dominated by the Poisson white noise. Although a strong red noise component emerges at $\lesssim 1$ mHz, we do not find any preferred periodicity in the analyzed range, including in particular at ~ 2.9 mHz which corresponds to 346 s.

As seen in figure 4.2, the source repeated spiky flares in the 1st half of the observation, and became much quiescent in the 2nd half. Therefore, we next calculated the Fourier power spectra for different time regions of this light curve. Red and blue traces in the same figure are the results for the first 8 ks (i.e., 3–11 ks in figure 4.2) and the remaining part of the light curve, respectively. The 1–10 mHz frequency regions of these spectra are expanded in the inset to figure 5.3(left). There, the power is still two orders of magnitude higher than would be expected for a pure Poissonian noise, implying that the red noise extends into these frequencies. Superposed on the red noise, the spectrum from the 1st 8 ks exhibits several noticeable peaks, including the highest one at 1.5 mHz, and the 2nd highest one at 2.9 mHz. As evident from the logarithmic top abscissa of the inset, they are apparently in the 1:2 harmonic ratio, and the 4th harmonic could also be seen at 5.6 mHz. This suggests the presence of a 1.5 mHz periodicity (together with its higher harmonics) in the 1st 8 ks of the data, and the 2.9 mHz feature (possibly the 2nd harmonic) could be identified with the 346-s periodicity.

It is however not easy to tell whether these peaks are real, or just due to fluctuations in the strong red noise. We hence adopt the technique by Israel and Stella (1996), which allows us to evaluate the significance of a suggested periodicity in a power spectrum where strong colored noise is present. It compares the power at a particular target frequency, with the local continuum estimated by averaging the spectrum on both (high-frequency and low-frequency) sides with logarithmically symmetric widths. Employing this technique with the smoothing width of 30 wave numbers, we obtained the results shown in the right panel of Figure 5.3. The smoothed power spectrum, plotted in blue, roughly follows a power-law function with an exponent of -1.5, which is typical of red noise. The red data points (with linear ordinate), obtained by dividing the raw power spectrum by the smoothed one, are confirmed to closely follow a χ^2 distribution with 2 degrees of freedom. This analysis might be affected by the smoothing width. Thus, we executed the Kolmogorov–Smirnov(KS) test for the χ^2 distribution with 2 degrees of freedom for various smoothing widths. The result is shown in figure 5.4. Israel and Stella assumed the χ^2 distribution when the p-value of $\gtrsim 0.1$, while our result has a p-value of ~ 0.3 at the smoothing width of 30. Therefore, we conclude that the normalized spectrum calculated with the smoothing width of 30 can be assumed as the χ^2 distribution.

There, we observe a series of prominent peaks, at 1.47, 2.93, 5.62, 9.03, and 11.72 mHz. Within the frequency resolution determined by the data length, their ratios, $1.00 : 1.99 : 3.82 : 6.14 : 7.97$, are consistent with the (mostly even) harmonic ratios 1:2:4:6:8. Among them, the one at 1.47 mHz, to be identified with the fundamental, is

obviously the feature noticed in the left panel, and has a chance-occurrence probability of $\mathcal{P}_1 = 0.0198$ before correcting for the frequency trials. The highest one at 11.72 mHz, regarded as the 8th harmonic, has a normalized power of 11.7, with the pre-trial probability of $\mathcal{P}_8 = 3.8 \times 10^{-3}$.

Let us suppose that the 1.47 mHz peak appeared due to a chance fluctuation, with a probability $\mathcal{P}_1$. Then, the probability to observe also the highest peak, at a frequency corresponding just to the 8th harmonic, should be $\mathcal{P}_1\mathcal{P}_8 = 7.5 \times 10^{-5}$. Further multiplying the frequency trial number, 121, we finally obtain the overall false alarm probability of 0.9%. Considering however the ambiguity in choosing the smoothing width, and uncertainties in treating the harmonics, we conservatively quote a probability of a few percent. We therefore conclude, with a confidence of $> 90\%$, that the source showed evidence of 1.47 mHz periodicity, or pulsation with a period of ~ 680 s, at least during the 1st 8 ks of the data. Incidentally, the chance probability would further decrease if we consider the simultaneous presence of the 2nd, 4th, and 6th harmonics, but this would be an overuse of the harmonic condition.

5.2.2 Periodogram analysis

Although we have obtained evidence for the 1.5 mHz periodicity, the limited frequency resolution does not allow an accurate period determination. Thus, following a standard procedure in pulsar studies, we next calculated chi-square periodograms using `efsearch` with 32 bins, over the frequency range of 1–10 mHz corresponding to the inset to figure 5.3, or equivalently, a period range of 100–1000 s, with a step of 0.1 s. The obtained results are shown in figure 5.5, where panels (1-a), (2-a), and (3-a) represent the entire data, the 1st 8 ks, and the latter 15 ks, respectively.

In agreement with the power spectra with the strong red noise, the obtained chi-square values are much larger than the degree of freedom, essentially at any period studied here. Furthermore, in panel (2-a) derived from the 1st 8 ks of the data, we observe several prominent peaks, although they are not recognized when we use the entire 23-ks data (panel 1), or those from the latter 15 ks (panel 3). The highest peak at ~ 675 s, of which the details are shown in panel (2-b), obviously corresponds to the 1.47 mHz periodicity found with the power spectrum. By fitting this peak with a cubic function, we determined the best period, or the maximum point of the probability distribution, as 674 s. A Gaussian fitting has given the same result. Although it is not straightforward to define the associated error, we conservatively quote a value of ± 15 s, as the half-width at half-maximum of the chi-square peak above the background.

In order to cross-check the result obtained using the normalized power spectrum, the significance evaluation was conducted also using the chi-square periodogram. For this purpose, we Fourier synthesized 1000 fake light curves, in which each Fourier amplitude is set to the square root of the normalized power obtained in the previous sub-section, whereas the associated Fourier phase is randomized. One of the examples of the fake light curve created in this simulation is shown in figure 5.6. We checked that a Fourier spectrum for this fake light curve is reminiscent of the original Fourier power spectrum. By analyzing the fake light curves in the same way as the actual data, we studied the probability of finding chi-square values, exceeding what was observed (about 1800), at the period of 674 s as shown in figure 5.6c. As a result, the chance occurrence probability was estimated as about 5%, which is consistent with the evaluation using the normalized power spectrum.

The periodogram in panel (2-a) also reveals several weaker peaks, including one at ~ 340 s which can be identified with the 2nd harmonic in our power spectrum.

Although the fundamental, which was rather weak in the power spectrum, has become dominant in the periodogram, the difference can be understood in the following way. In the normalized spectrum in figure 5.3 (right), the power is expressed all relative to the local red-noise intensity, so the fundamental becomes weaker due to the stronger local red noise. In contrast, the fundamental peak becomes prominent in the periodogram, because it sums over all the harmonics from $m = 1$ (fundamental) to $m = 16$ (the Nyquist frequency for 32 bin), whereas the 340 s peak is a sum over only $m = 2, 4, .., 16$. As a further attempt, we detrended the first 8 ks of the XMM-Newton light curve, using the 5th order polynomial. However, no major changes took place either in the power spectra or the periodograms.

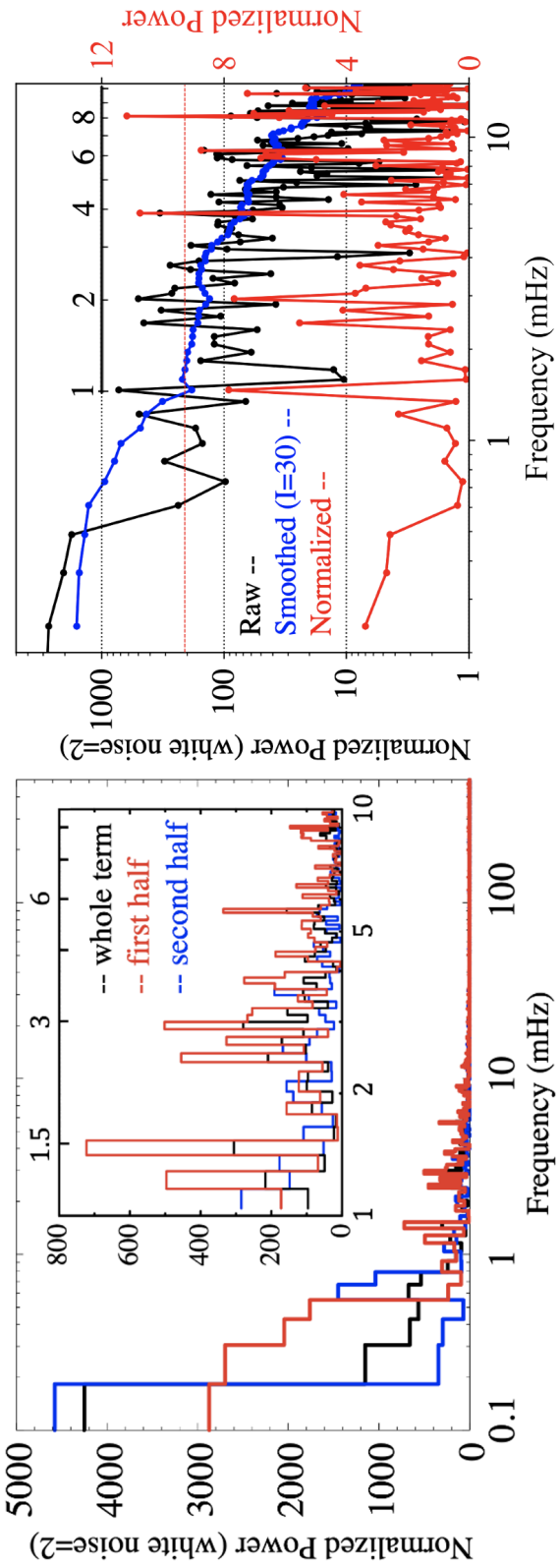

FIGURE 5.3: (Left) Fourier power spectra for the whole (black), the first 8 ks (red), and the remaining part (blue) of the XMM-Newton/PN light curve. The abscissa is logarithmic, in order to reveal low-frequency structures. The inset is the enlarged view of the spectra in the 1–10 mHz range, where the logarithmic tick marks at the top abscissa are drawn at multiples of 1.5 mHz. (Right) Evaluation of the power spectrum from the first 8 ks, using the technique by Israel and Stella (1996). The raw spectrum in black (the same as red in the left panel) is averaged over 30 data points, into a smoothed spectrum shown in blue. Both use logarithmic ordinate. The red solid line presents the normalized spectrum, where the raw spectrum is divided by the smoothed one. It refers to the linear ordinate on the right, and the inset abscissa shows the harmonic numbers. The horizontal dashed line in red indicates the 99% confidence level for a single trial.

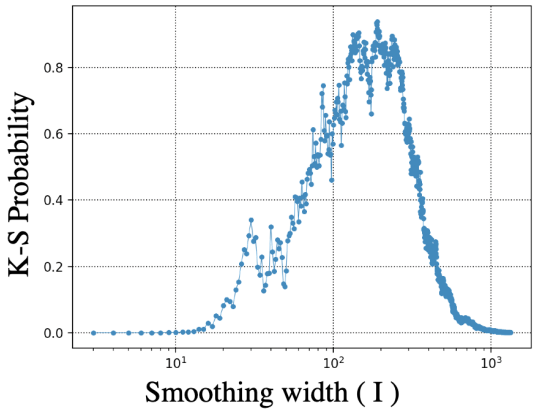

FIGURE 5.4: K-S probability distribution of the log-normalized Fourier spectrum for a chi-square distribution with the d.o.f of 2 for various smoothing widths (I).

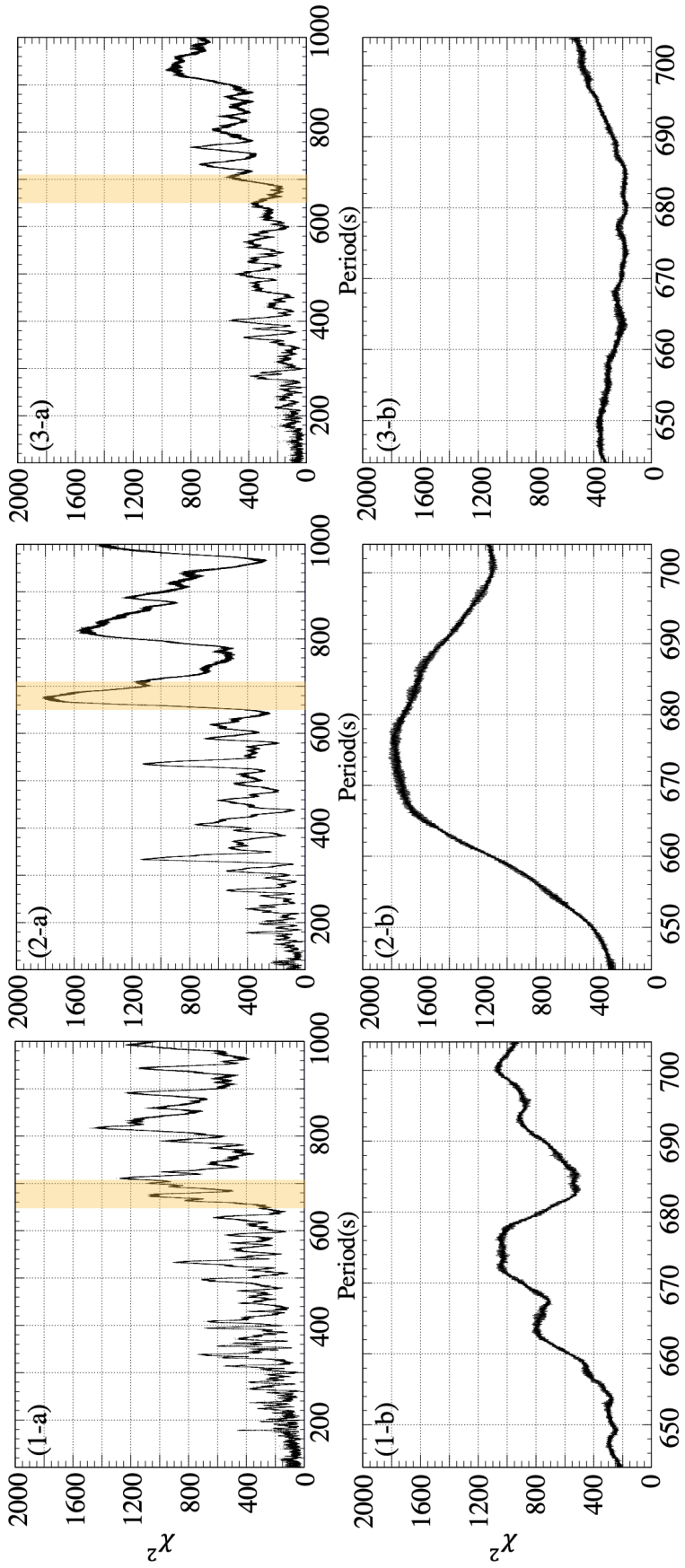

FIGURE 5.5: Chi-square periodograms with 32 bins, derived from (1-a) the whole data, (2-a) the first 8 ks, and (3-a) the latter 15 ks. Panels (1-b) to (3-b) expands these periodograms over a period range of 645–705 s.

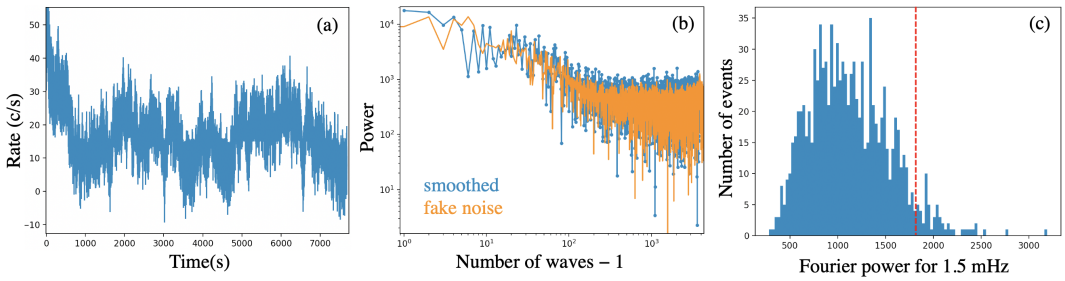

FIGURE 5.6: The intermediate output for the phase randomization technique. (a) is an example of the fake light curve. (b) is the Fourier power spectrum for the fake light curve(orange). The smoothed power spectrum for the real light curve is also shown for reference. (c) is a histogram for the Fourier powers at 1.5 mHz, obtained by 1000 simulations. The red dashed line indicates the peak height of the peak at 1.5 mHz in the Fourier power spectrum and is consistent with an accumulative distribution function of 5.4%.

5.2.3 Folded pulse profiles

For a further confirmation of the results derived so far, we inspected the original light curve in figure 4.2, and found that sharp intensity minima repeat at about 674 s, as indicated by thin vertical lines over the relevant portion of the data. Therefore, the periodicity is considered to have good coherence. In addition, such sharp intensity drops are likely to arise via geometrical effects (e.g., self eclipse of the emission region) related to the rotation of the compact object (a NS in this scenario). This makes a contrast to the case of flares, which would occur either at a specific rotation phase of the compact star, or in a manner unrelated to the rotation (e.g., caused by quasi-periodic blobs in the stellar winds). Therefore, we regard the 674-s period as a strong candidate for the pulse period of this X-ray source. Its relation to the previously reported 346-s period is considered in sub-section 6.1.2.

Figure 5.7 shows the pulse profile, obtained by folding the 0.1–15.0 keV data from the 1st 8 ks at the period of 674 s. The pulse profile is rather structured, in a qualitative agreement with the emergence of up to the $m = 8$ harmonics in figure 5.3 (right). In addition, the profile is double-peaked, consisting of a pair of large and small peaks which are about half a cycle apart. This explains why the even higher harmonics are strong in the power spectra (either raw or normalized).

5.3 Analysis of the brighter spectra

To constrain the nature of the compact object of IGR J00370+6122 from X-ray spectral viewpoints, we analyzed 1-10 keV energy spectra obtained by the XMM-Newton/EPIC, the Suzaku/XIS, and the Swift/XRT. Below, errors and upper limits of the spectral parameters. as well as those on fluxes and luminosities, all refer to 90% confidence levels.

We first analyze the PN/MOS1/MOS2 spectra, acquired in the XMM-Newton observation in the flaring state (figure 4.2). The data have the highest statistics, and have allowed us to detect the 674-s tentative pulse period. Because the spectra derived from the 1st 8 ks and the latter 15 ks do not show significant differences (except that in the normalization), below we employ the entire data. As presented in figure 5.8a and table 2, a simple power-law model with absorption (`phabs * powerlaw`) approximately reproduced the spectra, incorporating a rather hard photon index of

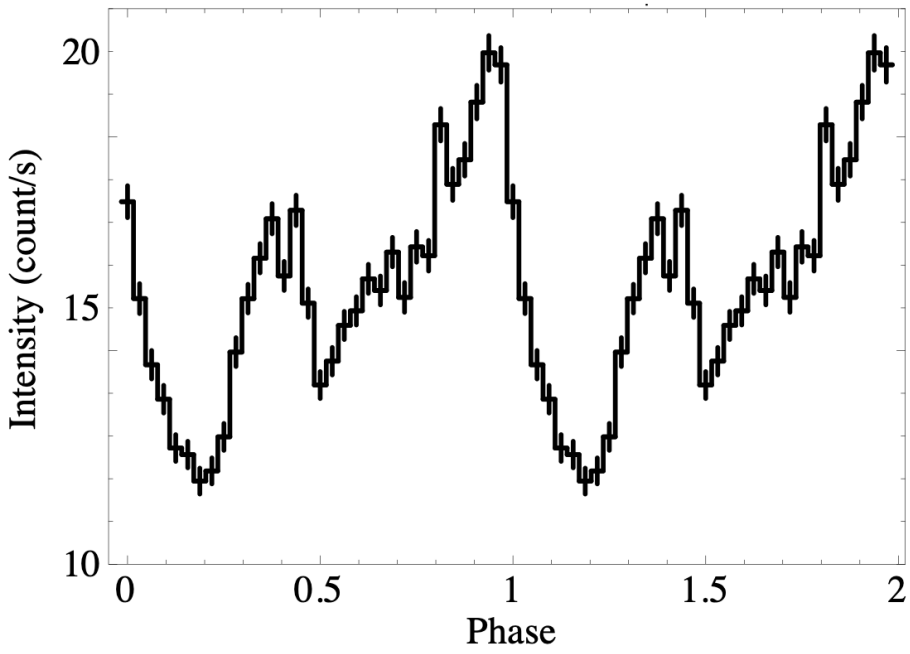

FIGURE 5.7: The 0.1–15 keV EPIC/PN data from the 1st 8 ks of the XMM-Newton observation, folded at 674 s.

$\Gamma \sim 1.2$. However, the fit was unacceptable due to residuals at < 2 keV and > 7 keV. When we employ a cutoff power-law model instead, the residuals have disappeared and the fit has become acceptable (table 2). The derived photon index is even harder, $\Gamma \sim 0$, and the cutoff energy is obtained as $E_{\rm cut} \sim 3.7$ keV.

The Suzaku/XIS data were obtained for 60 ks in quiescence, when the source was about 40 times fainter than in the flaring-state XMM-Newton observation. The source exhibited small (a factor of < 4) variability, without significant pulsations. As presented in figure 5.8b and table 2, the time-averaged 1–10 keV XIS spectra were reproduced reasonably well by the simple absorbed power-law model, with a softer photon index of $\Gamma \sim 2$. When we apply the cutoff factor to the power-law continuum, the fit has been improved, with a decrease in chi-square by about 30, and the cutoff energy has been constrained as $E_{\rm cut} \sim 3$ keV (table 2 for details).

The Swift/XRT data sets have a typical exposure of a few kiloseconds each. Although some of these data sets, particularly those when the source is active, showed factor 3–10 intensity variations within each, we again analyze the spectra which are averaged over individual observations. Among the 31 data sets altogether, nine (all acquired in flaring activity and near the periastron) have statistics which are high enough for the spectral studies. As summarized in table 2, these 9 spectra have all been reproduced successfully by the absorbed power-law model. Figure 5.8c shows the brightest five spectra.

In figure 5.8c, we observe a spectral change with a "harder when brighter" trend; the spectrum becomes harder (Γ gets smaller) when the source flux becomes higher. For a further confirmation of this property, figure 5.9 shows a scatter plot between Γ and the 1–10 keV flux, obtained with the XMM-Newton/EPIC, the Suzaku/XIS, and the Swift/XRT (the 9 data sets). Thus, the "harder when brighter" property is clearly confirmed.

As in table 2, the absorbing column density $N_{\rm H}$ was relatively constant at about 1×10^{22} cm^{-2}, when the spectra from the different instruments are fitted individually with a power-law continuum. Since the high-statistics XMM-Newton spectra

(ObsID=501450101) require a cutoff power-law continuum and a lower $N_{\rm H}$ value, the actual absorption column density might be at around 0.7×10^{22} cm^{-2}.

5.4 Analysis of the fainter spectra

We have so far analyzed 11 spectra, one from XMM-Newton, another from Suzaku, and 9 from the Swit/XRT. We still have one more XMM-Newton data set (the 2nd observation) when the source was very faint and was only in the MOS2 field-of-view, and 22 Swift/XRT spectra acquired at orbital phases rather away from the periastron. Although these data would not have statistics high enough to constrain the spectral properties, they are still useful when we study how the flux depends on the orbital phase. In dealing with these data, we fitted simultaneously the source+background spectrum and the background spectrum, because some data bins would become negative if we directly subtracted the background. The source spectrum was modeled by a simple absorbed power-law, with $\Gamma = 2.06$ and $N_{\rm H} = 1.26 \times 10^{22}$ cm^{-2} both fixed, referring to the Suzaku/XIS determinations. The background spectrum was derived from an outer region in the same detector, and was modeled by an unabsorbed power-law, with the photon index fixed at $\Gamma = 0.20$ for the XMM-Newton/EPIC spectrum and $\Gamma = 0.64$ for those with the Swift/XRT. In each spectral fitting, only the normalizations of the source and background components were set free. The fit goodness was evaluated with the Poisson statics (C-stat in `XSPEC`, Cash, 1979), instead of the chi-square criterion.

In the 2nd XMM-Newton observation (ObsID 0742800201), with a net exposure of 11 ks, we detected only 26 source+background events, and 13 events in the background region. From these, we obtained a 1–10 keV flux of $(8^{+5}_{-4}) \times 10^{-14}$ erg cm^{-2} s^{-1}, which corresponds to a luminosity of $(1.1^{+0.7}_{-0.5}) \times 10^{33}$ erg s^{-1} at 3.4 kpc. Similarly, by analyzing the fainter 22 Swift/XRT spectra in this way, we positively detected the source in 17 observations, and derived upper limits in the remaining 5 cases. In all of them, the 1–10 keV luminosity was $\lesssim 10^{34}$ erg s^{-1}. The derived luminosities (including the upper limits) are utilized later in our examination of the orbital luminosity modulation.

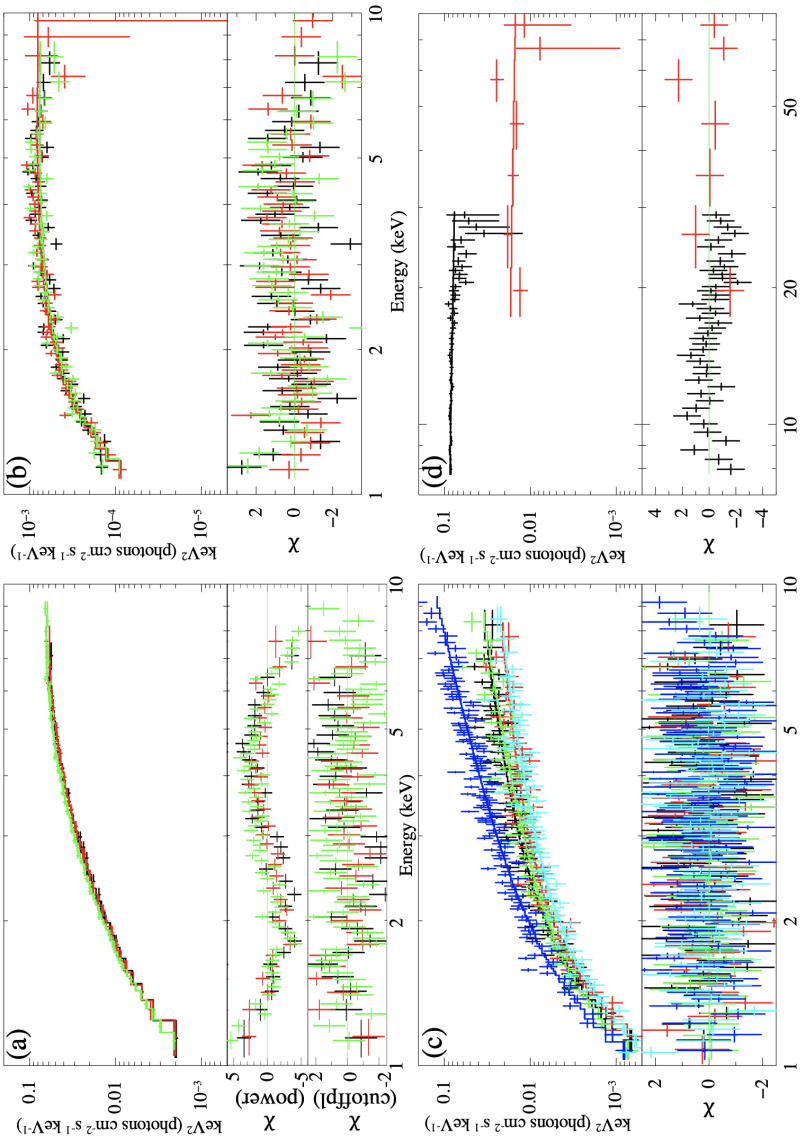

FIGURE 5.8: Model fitting results to the spectra of IGR J00370+6122, presented in the $\nu F\nu$ form. (a) The EPIC MOS1 (black), MOS2 (red), and PN (green) spectra, obtained in the flaring-state XMM-Newton observation, and fitted simultaneously with an absorbed power-law model. The middle and bottom panels show residuals from the power-law fit and the cutoff power-law fit, respectively, both with absorption. (b) The Suzaku XIS0 (black), XIS1(red), and XIS3 (green) spectra, fitted simultaneously with an absorbed power-law model. The fit residuals are given in the bottom panel. (c) The brightest 5 spectra from the Swift/XRT, fitted individually by an absorbed power-law model. (d) Combined spectra with the RXTE/PCA (black) and the INTEGRAL/ISGRI (red). They were obtained both near the periastron, but not simultaneous.

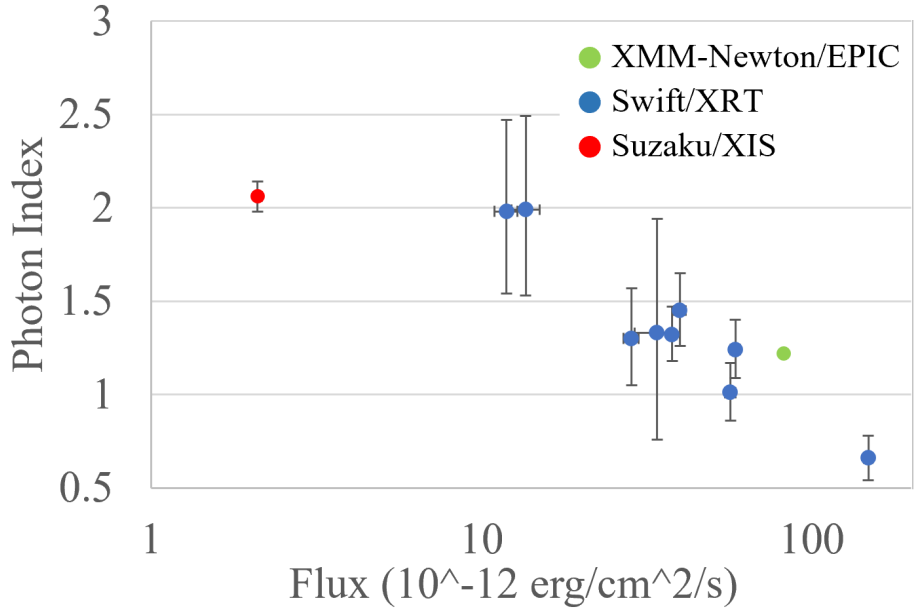

FIGURE 5.9: A Scattered plot between the photon index (from the power-law fit) and the 1–10 keV flux. Data points refer to those presented in Table 5.1, i.e., relatively bright data where the spectral shapes have been constrained.

TABLE 5.1: Results of the spectral fitting, using the absorbed power-law and cutoff power-law models.

Instruments	ObsID	Flux*	$N_{\rm H}$ (10^{22} cm^2)	Γ	$E_{\rm cutoff}$	χ^2/d.o.f
RXTE	91061010101†	220	9.1±0.3	2.14±0.02	–	–
XMM-Newton	0501450101	83.50	1.16	1.22	–	1558.09/273
	0501450101§	$79.82^{+2.74}_{-2.64}$	$0.62^{+0.03}_{-0.03}$	$0.05^{+0.06}_{-0.06}$	$3.70^{+0.19}_{-0.17}$	316.79/272
Suzaku	402064010	$2.08^{+0.28}_{-0.25}$	$1.29^{+0.11}_{-0.11}$	$2.06^{+0.08}_{-0.08}$	–	193.25/147
	402064010§	$1.97^{+0.53}_{-0.41}$	$0.67^{+0.21}_{-0.20}$	$0.50^{+0.47}_{-0.47}$	$2.79^{+1.19}_{-0.65}$	161.62/146
Swift	00032620005	$58.70^{+1.88}_{-2.00}$	$1.35^{+0.23}_{-0.21}$	$1.24^{+0.16}_{-0.15}$	–	84.32/78
	00032620009	$39.92^{+1.63}_{-1.69}$	$1.45^{+0.29}_{-0.26}$	$1.45^{+0.20}_{-0.19}$	–	58.47/62
	00032620013	$11.92^{+0.91}_{-0.95}$	$2.09^{+0.84}_{-0.73}$	$1.98^{+0.49}_{-0.44}$	–	15.67/14
	00032620015	$13.62^{+1.36}_{-1.28}$	$2.90^{+0.90}_{-0.79}$	$1.99^{+0.50}_{-0.46}$	–	18.90/19
	00032620019	$56.75^{+2.11}_{-2.20}$	$0.82^{+0.19}_{-0.17}$	$1.01^{+0.16}_{-0.15}$	–	68.47/76
	00032620028	$34.04^{+5.75}_{-4.97}$	$1.88^{+1.02}_{-0.89}$	$1.33^{+0.61}_{-0.57}$	–	7.77/13
	00032620029	$28.47^{+1.42}_{-1.50}$	$1.96^{+0.51}_{-0.45}$	$1.30^{+0.27}_{-0.25}$	–	39.92/35
	00032620030	$148.48^{+4.31}_{-4.47}$	$1.03^{+0.18}_{-0.16}$	$0.66^{+0.12}_{-0.12}$	–	114.42/129
	00032620031	$37.79^{+1.15}_{-1.21}$	$1.32^{+0.20}_{-0.18}$	$1.32^{+0.15}_{-0.14}$	–	58.35/88

* Unabsorbed fluxes in 1–10 keV (3–20 keV for the RXTE/PCA data), in units of 10^{-12} erg s^{-1} cm^{-2}.

† Parameters refer to in 't Zand et al., 2007 for 3-20 keV.

§ Fitting results with the cutoff power-law model.

5.5 High-energy spectral properties in bright phases

To characterize the spectrum at higher energies when the source is near the periastron and is hence bright, we analyzed the RXTE/PCA (10–30 keV) and INTEGRAL/ISGRI (17.3–80 keV) data. The former was derived from standard data products for ObsID=91061-01-01-01, which caught a flaring activity at an orbital phase of an orbital phase of ∼0.05 (or ∼0.14 in our phase definition in Table 4.1) and enabled the detection of the 346-sec period (in 't Zand et al., 2007). The utilized INTEGRAL/ISGRI data cover a 10-year period of 2003–2012, but we selected the events only in the orbital phase interval from –0.1 to 0.1 where the source is significantly bright in figure 5.2. The RXTE/PCA and INTEGRAL/ISGRI spectra were fitted with a single power-law function without absorption. The fit is simultaneous, except the spectral normalization which is allowed to take separate values between the two spectra considering that they are not simultaneous. As shown in figure 5.8d, the fit was successful with a reduced chi-square of 0.99, and gave a flat continuum with a photon index of 2.09 ± 0.04. We also tried a cutoff power-law fit, in order to constrain a possible spectral turn-over which is observed in many other HMXBs. However, the fit (which was already acceptable) did not improved significantly, and a 90% confidence limit of $E_{\rm cut} > 38.6$ keV was derived. Thus, the 10–80 keV spectrum of IGR J00370+6122 can be explained by a $\Gamma \sim 2.1$ power-law without significant high-energy cutoff.

Chapter 6

Discussion

6.1 The nature of the compact object in IGR J00370+6122

In order to better understand the nature of the compact component in the HMXB IGR J00370+6122, we analyzed various X-ray archival data, obtained with the 6 X-ray instruments onboard altogether 5 missions. These data sets differ in many attributes such as the sensitivity, energy range, observation epoch, time length, orbital-phase coverage, and the source intensity during the observation. Their comprehensive analysis has enabled us to deepen our understanding of this object. Below, we summarize the obtained results from the timing and spectral aspects.

6.1.1 Timing results: orbital intensity variations

Our analysis of the 15–50 keV Swift/BAT data, covering a 15 yr period of 2005–2019, yielded the following three results. First, the orbital period has been refined as in equation (5.1). Second, as already reported by in 't Zand et al., 2007, the orbit-folded light curve in figure 5.2 shows a strong orbital modulation, that the X-ray emission is strongly enhanced over a limited orbital phase from -0.1 to 0.2. Finally, the same figure reveals a slight (~ 0.05 cycle) delay of the X-ray intensity maximum from the periastron passage, in broad agreement with Grunhut, Bolton, and McSwain, 2014 and González-Galán et al., 2014.

Although the second result above is of importance, the limited Swift/BAT sensitivity hampers us to infer from figure 5.2 to what extent the source gets dim when it is away from the periastron. To understand this issue, in figure 6.1 we plot all the flux measurements from the present study, except those with the Swift/BAT, as a function of the orbital phase. Thus, away from the periastron phases, the source has been found to decline to extreme low luminosities, down to $\sim 10^{32}$ erg s^{-1}, almost by 3 orders of magnitude from the periastron phases. This behavior is likely to repeat regularly each orbital cycle, because it is consistently indicated by the relatively dense sampling with the Swift/XRT, as well as by the Suzaku and the 2nd XMM-Newton observations. In addition, we find a hint of a rather abrupt luminosity drop at an orbital phase of ~ 0.3, and possibly a quick return at a phase of ~ 0.95. Later, we try to theoretically explain this behavior.

6.1.2 Timing results: the possible pulse detection

To reconfirm the pulsation that was detected only once in the past by the RXTE/PCA, we searched for a pulsation using the 2008 XMM-Newton data, which are suitable for this purpose because the object was rather bright and flare active as in the RXTE observation, and the data have a longer exposure (23 ks vs 4 ks). As a result, a candidate period has been discovered at 674 ± 15 s.

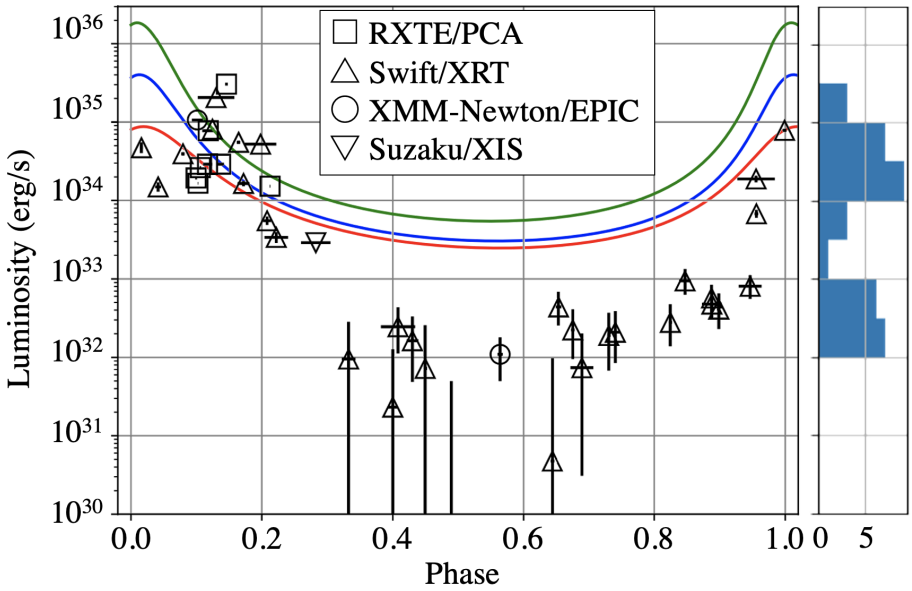

FIGURE 6.1: Orbital variations of the X-ray luminosity of IGR J00370+6122. The data points of Swift/XRT, XMM-Newton/EPIC and Suzaku/XIS are from the present analyzes, while RXTE/PCA ones are from in 't Zand et al., 2007. Three solid curves are theoretical predictions (see text), calculated for the stellar mass/eccentricity of (red) $22M_{\odot}/0.48$, (blue) $15M_{\odot}/0.56$, and (green) $8M_{\odot}/0.56$, referring to Grunhut, Bolton, and McSwain, 2014, González-Galán et al., 2014 and Hainich et al., 2020, respectively. The right histogram shows the distribution of the measured luminosities excluding upper limits.

in 't Zand et al., 2007 in fact found, in their RXTE periodogram, not only the 346 s peak which they favor, but also a broad enhancement at about 700 s (which is higher than the 346 s peak) and 550 s. Therefore, the two observations consistently prefer three common periods; 340-346 s, $\sim$ 550 s, and 674–700. Although the nature of the $\sim$ 550 s enhancement is unclear, the other two periods can most naturally be regarded as the fundamental and the 2nd harmonic, as we already argued repeatedly. If the folded pulse profile is mildly time variable, the major and minor peaks in figure 5.7 could sometimes have comparable intensities, to make the pulse period appear to be $\sim$ 340 s. In fact, the X-ray pulsar Vela X-1 was first thought to have a pulse period of about 141 s, but the period was later revised as 283 s (Mcclintock et al., 1976).

6.1.3 Spectral results

Next, the energy spectral analyzes were performed to characterize IGR J00370+6122 from spectral viewpoints. The 1-10 keV energy spectra obtained by the XMM-Newton/EPIC, the Suzaku/XIS, and the Swift/XRT were approximately represented by an absorbed power-law model. Furthermore, a mild spectral cutoff with $E_{\rm cutoff} = 3 - 4$ keV, together with a very hard spectral slope with $\Gamma = 0 - 0.5$, are indicated by the XMM-Newton spectrum, and by the Suzaku data to a lesser extent. The absorption column density was stable at $N_{\rm H} \sim 1 \times 10^{22}$ cm^{-2}. Since the optical companion, BD+60 73, has an optical extinction of $A_{\rm v} = 2.39$ (González-Galán et al., 2014; Hainich et al., 2020), the Galactic line-of-sight column is estimated as $N_{\rm H} \sim (5 - 6) \times 10^{21}$ cm^{-2}, which is consistent with the Galactic coordinates of IGR J00370+6122, $(\ell, b) = (121^{\circ}.2, -1^{\circ}.5)$, and its distance. Thus, the observed $N_{\rm H}$ is

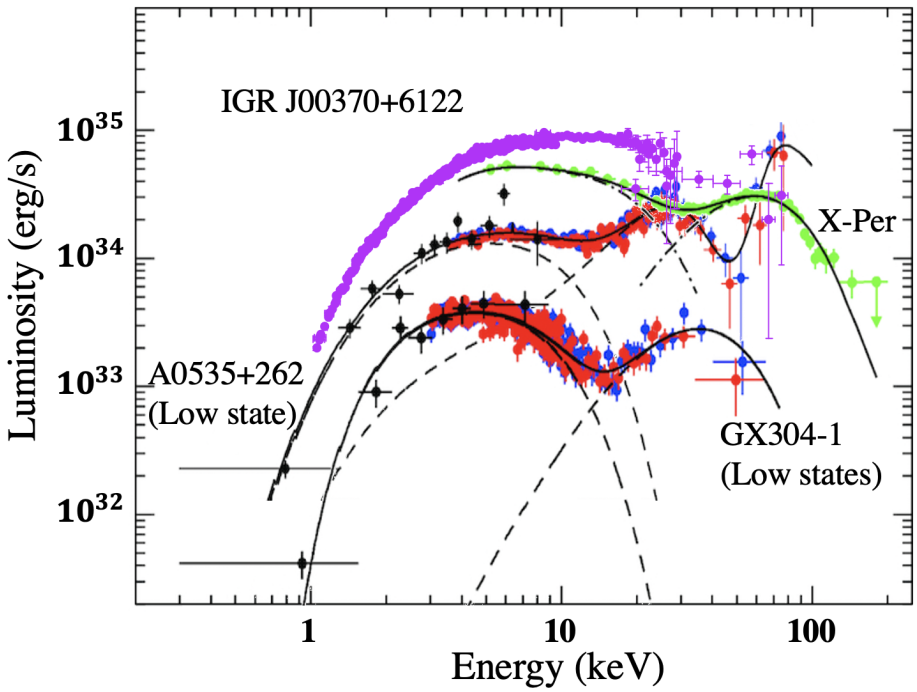

FIGURE 6.2: A combined spectrum with XMM-Newton/EPIC, RXTE/PCA and INTEGRAL/ISGRI of IGR J00370+6122 is compared with those of X Persei, A0535+26 and GX304-1 adapted from Doroshenko, V. et al. (2012), Tsygankov et al. (2019a) and Tsygankov et al. (2019b). For IGR J00370+6122, the XMM-Newton/MOS2, PN, RXTE/PCA and INTEGRAL/ISGRI spectra are renormalized in reference to the XMM-Newton/MOS1 spectrum.

likely to be a mixture of about equal Galactic and circum-source contributions. Analyzing the 3–20 keV RXTE/PCA spectrum with an absorbed power-law model, in 't Zand et al., 2007 derived $N_{\rm H} \sim 10^{23}$ cm^{-2} (table 5.1), which is an order of magnitude higher than those we have obtained. This discrepancy probably arose because the intrinsic spectral curvature was mimicked by the strong absorption, when the RXTE/PCA spectrum above 3 keV was fitted with a single power-law.

6.1.4 Identification of the compact object in IGR J00370+6122

Even though the evidence for the 674-s pulsation gives a strong support to the argument for a magnetized NS in this system, we are still left with a few percent probability that the detection is false. In addition, the pulsation was detected only from a limited portion of the XMM-Newton observation. Similarly, the evidence for pulsation had been obtained only once, out of a number of past observations. Therefore, we need to carefully examine whether our interpretation can be supported from other pieces of evidence.

Starting our examination from a basic viewpoint, the compact object in IGR J00370+6122 must be either a white dwarf, a black hole (BH), or a NS. The maximum luminosity of $\sim 10^{35}$ erg s^{-1} and the 674-s pulsation (assuming it to be real) are both explicable in terms of a white dwarf. However, it would be extremely unlikely that a white dwarf ever formed a binary with a massive star. The observed spectrum, with weak or no emission lines, also disagrees with line-rich thermal spectra from accreting white dwarfs. Therefore, the white dwarf scenario can be readily ruled out.

Let us next consider a possibility that the compact star is a BH. In fact, the observed violent variability and the relatively hard spectra both broadly agree with those of accreting BHs. If so, however, the luminosity of this object, 10^{35} erg s^{-1} when it is bright, would translate to 0.02% of the Eddington luminosity for a typical BH mass of 5 $M_\odot$. Then, the BH would have to be in the low/hard state, wherein the spectrum from a few keV to a few tens keV should be approximated by a $\Gamma \sim 1.7$ power law, accompanied by a clear cutoff with $E_{\rm cutoff} = 50-150$ keV (e.g., Makishima et al., 2008). The observed spectrum of IGR J00370+6122 is clearly distinct, harder than this in < 10 keV, and softer but possibly less curved in > 10 keV. Thus, the compact object cannot be considered as a BH, either.

As a result, we are left with the sole option that the compact object is a NS. In this case, we still have to tell whether the NS is strongly magnetized with the MFs $B \gtrsim 10^{12}$ G, or has relatively weak MFs as $B \lesssim 10^9$ G. Clearly, the former is favored for a few reasons. First, as an old stellar population, weak-field NSs form binaries predominantly with low-mass stars, and rarely with massive ones. (Probably IGR J00370+6122 is located on the Perseus arm.) Second, the former type of objects often exhibit flare-like variations like those seen in IGR J00370+6122 on time scales of minutes, whereas the latter objects, when dim, vary randomly on times scales of minutes to hours, but more continuously, typically with a relative amplitude of $\sim 20\%$ (e.g., Takahashi, Sakurai, and Makishima, 2011). Finally, the spectrum of IGR J00370+6122 is very similar to those of binary X-ray pulsars (see next subsection), whereas distinct from those of weak-MF NSs (e.g., Ono et al., 2017) which are more similar to those of BHs in the low/hard state. Therefore, independently of the 674-s periodicity, our comprehensive study supports the presence of a high-MF NS in IGR J00370+6122.

6.2 Comparison with the known binary X-ray pulsars

Taking it for granted that the compact object in IGR J00370+6122 is a magnetized NS, our next task is to compare it with the known binary X-ray pulsars, particularly those with low luminosities, to understand its properties and behavior as a mass-accreting NS.

6.2.1 General similarities

We have successfully quantified the 1–10 keV spectra of IGR J00370+6122 over a rather wide luminosity range as seen in figure 5.8, and found that the photon index becomes harder from 2 to < 1 as the luminosity increases from 3×10^{33} to 2×10^{35} erg s^{-1} (figure 5.9). This spectral behavior, "harder when brighter", and the very hard photon index of < 1, agree with the properties observed from nine Be-type X-ray pulsars when they are < 0.1 times the Eddington luminosity (Reig & Nespoli 2013). This similarity provides yet another supporting evidence that IGR J00370+6122 is an accreting magnetized NS. The "harder when brighter" trend, consistently observed from these low-luminosity pulsars (including IGR J00370+6122), may be explained as a spectral hardening caused by an increase of the inverse-Compton scattering probability, in response to the increase in the accretion rate (Ballhausen, Ralf et al., 2017).

Here, we discussed the X-ray emission mechanism of IGR J00370+6122. Among the facts about the parameters obtained from the spectral analysis, the following are considered to be related to the X-ray emission mechanism. (1) There is no significant change in $N_{\rm H}$ in all observed data. (2) The flat $\nu F\nu$ spectrum of $\Gamma \sim 2$ was observed

at the Suzaku observation. (3) The specific exponents of $\Gamma \sim 1.3$ were observed from some of the Swift and XMM-newton spectra. From the observational fact (1), the "harder when brighter" trend might not be ostensibly caused by a change of $N_{\rm H}$. The flat spectral feature, observational fact (2), indicates that the spectra of this object cannot reproduce by the thermal emission of a single electron temperature. The fact (3) indicates that the possibility of the bremsstrahlung emission as seed photons. This fact leads us to evoke that the X-ray emission is not generated at the denser region (i.e NS surface) but inside the accretion column. Considering all observational facts, the possible X-ray emission process is as follows. The seed photons generated in the accretion column by bremsstrahlung will be inverse-Comptonized inside the accretion column and this forms the high-energy component in IGR J00370+6122 spectrum. This model can easily explain the "harder when brighter" trend by the increase of the Compton scattering probability as the increase of accretion rate. The Compton y-parameter, calculated by a future follow-up observation with high statistics, can reveal that the feasibility of this model.

We find several additional similarities between IGR J00370+6122 and Be-type pulsars. These include the large orbital intensity changes (figure 6.1), the small but significant difference between the peak-brightness and periastron phases (figure 5.2), and the weakness of iron-K emission line (figure 5.8). Considering further the lack of a circumstellar disk (Reig et al., 2005) in the primary BD+60 73, its stellar winds may be somewhat anisotropic, and denser along equatorial directions of its rotation.

As seen so far, the magnetized-NS interpretation is supported, not only via the elimination argument, but also by general similarities seen between IGR J00370+6122 and the known binary X-ray pulsars (particularly of Be companions).

6.2.2 Magnetic fields and spin periods

Using the RXTE/PCA and INTEGRAL/ISGRI data (though not simultaneous), we have found that the high-energy spectrum of IGR J00370+6122 extends up to 80 keV with a photon index of $\Gamma \sim 2.2$, without noticeable cutoff. Combined with the information below 10 keV from XMM-Newton, Suzku, and Swift, the X-ray spectrum of IGR J00370+6122 is hence found to keep a rather flat shape over nearly two orders of magnitude in energy. Actually, the constraint of $E_{\rm cutoff} > 38.6$ keV derived for IGR J00370+6122 is considerably higher than the values of $E_{\rm cutoff} = 5 - 10$ keV measured from binary X-ray pulsars at a typical luminosity of $\sim 10^{37}$ erg s^{-1}. This difference may be attributed to the very low luminosity of IGR J00370+6122, $\sim 1 \times 10^{35}$ erg s^{-1}, or 0.1% of the Eddington luminosity for a NS with 1.4 $M_{\odot}$, even though it refers to the brightest phase near the periastron.

To examine the above possibility, we compare in figure 6.2 the broad-band spectrum of IGR J00370+6122 with those of three binary X-ray pulsars with comparable low luminosities, all having Be-type optical companions. One is the nearby binary X-ray pulsar X Persei, which has a persistently low luminosity (Doroshenko, V. et al., 2012; Tsygankov et al., 2019a; Tsygankov et al., 2019b; Yatabe et al., 2018). The other two are typical recurrent Be-type transients, A0535+26 and GX 304 − 1, which were recently observed in a very X-ray dim phase during a decay phase of their outbursts (Ballhausen, Ralf et al., 2017; Tsygankov et al., 2019b). Thus, the most outstanding spectral property common to the four objects is the hard X-ray continua that extend with a flatter shape to higher energies, than those of more luminous accreting pulsars which strongly turn over at $\gtrsim 20$ keV. Therefore, the flat spectrum of IGR J00370+6122 may be explained, at least partially, as a property which is common to dim X-ray pulsars, even though its mechanism is unclear at present.

Another noticeable property in figure 6.2, which is particularly prominent in A0535+26 and GX 304 − 1, is a two-hump structure of the spectrum, with two peaks at a few keV and a few tens keV, as already pointed out by Tsygankov et al., 2019a and Tsygankov et al., 2019b. (In A0535+26, another sharp dip at 50 keV is due to the CRSF; Terada et al., 2007). This two-hump structure is possibly present in X Persei and in IGR J00370+6122 as well, but less visible. Among the three comparison objects, A0530+26 and GX 304 − 1 have surface MFs of $B \sim 4.5 \times 10^{12}$ G and $\sim 5.5 \times 10^{12}$ G, respectively, as measured securely with their CRSFs. In contrast, X Persei has a considerably stronger dipole MF of $B \sim 10^{14}$ G, as estimated through the GL79 modeling (Introduction; Yatabe et al., 2018) which has been verified and calibrated quantitatively using long-term MAXI observations (Sugizaki et al., 2015; Takagi et al., 2016; Sugizaki et al., 2017; Sugizaki et al., 2020). Then, the closer resemblance of the IGR J00370+6122 spectrum to that of X Persei, than to those of the two recurrent transients, suggest that IGR J00370+6122 also has a MF of $> 10^{13}$ G, as already suggested by Grunhut, Bolton, and McSwain (2014). This inference is also supported by an empirical positive dependence of $E_{\rm cutoff}$ on the CRSF energy (Makishima et al., 1999); this dependence may be explained theoretically in terms of cyclotron resonance cooling in the accretion column which will shift to higher energies for stronger MFs.

Interestingly, the three comparison objects in figure 6.2 have relatively long spin periods on the order of 100 s or longer. Other examples of low-luminosity pulsars with hard flat spectra and very long periods include 4U 0114+65 (with a period of 9340 s), 4U 1954+317 ($\sim 2 \times 10^4$ s), and 4U 2206+54 (5540 s). In contrast, the Be pulsars with fast rotation, 4U 0115+63 (3.6 s) and X0331+53 (V0332+53; 4.4 s), show rather softer spectra when they are dim at $\lesssim 10^{34}$ erg s^{-1} (Wijnands & Degenaar 2016). Therefore, an X-ray pulsar with a low luminosity and a hard continuum spectrum tends to have a long spin period. This empirical tendency suggests IGR J00370+6122 to have a long spin period as well, and reinforces the case for the 674-s pulsation.

Yet another class of accreting NSs to be considered for comparison are SFXTs (Sidoli, 2017) as introduced in section 1.4.3. Indeed, IGR J00370+6122 has several similarities to them, including the sharp X-ray flares on time scales of several minutes, a large dynamic range ($\sim 10^3$) in the intensity distribution, long quiescent phases (duty cycle of $\gtrsim 95\%$), and the very low time-averaged X-ray luminosity ($\lesssim 10^{34}$ erg^{-1} s^{-1}). However, the dynamic range of IGR J00370+6122 is not necessarily as large as those (up to $\sim 10^5$) of the most typical SFXTs. Therefore, from the X-ray observations, IGR J00370+6122 may be regarded as a system in between the classical HMXB and SFXT. IGR J00370+6122, located at the Galactic longitude of $\sim 120°$, allows detailed optical observations, in contrast to SFXTs which are optically highly obscured. Supposing that IGR J00370+6122 is similar to SFXTs, the information to be obtained from future observations of BD+60 73 will add to our understanding of SFXTs as well.

6.3 The luminosity change along the orbit and magnetic propeller effects

As discussed in sub-subsection 6.1.1, we have found that the luminosity of IGR J00370+6122 changes along the orbit by a large dynamic range reaching three orders of magnitude (figure 6.1). We further notice an abrupt luminosity drop at the orbital phase ~ 0.3, from $\sim 4 \times 10^{33}$ to $\sim 1 \times 10^{32}$ erg s^{-1}, and possibly a reversal at

the orbital phase ~ 0.95. Let us numerically examine whether this behavior can be explained by a standard scenario of the wind-capture accretion.

Presuming that the NS in IGR J00370+6122 is powered by capturing the stellar winds from the massive primary, we employ a simple Hoyle-Lyttleton accretion picture, taking into account the orbital phase dependence of the wind capture rate (Wind-Rose effect, Natalya & Lipunov 1998). In this picture, the mass accretion rate $\dot{M}_{\rm acc}$ onto the NS is assumed as

$$\dot{M}_{\rm acc} = \frac{1}{4}\left(\frac{R_{\rm cap}}{r}\right)^2 \left(\frac{v_{\rm rel}}{v_{\rm w}}\right) \dot{M}_{\rm w} \ . \tag{6.1}$$

Here, r is the distance of the NS from the primary star, $\dot{M}_{\rm w}$ is the primary's wind mass loss rate, $v_{\rm rel}$ is the relative velocity between the NS and the local stellar wind, $v_{\rm w}$ is the stellar-wind velocity at the position of the NS, and $R_{\rm cap}$ is the gravitational wind-capture radius defined as

$$R_{\rm cap} = \frac{2GM_{\rm NS}}{v_{\rm rel}^2} \ , \tag{6.2}$$

where G is the gravitational constant, and $M_{\rm NS}$ is the NS mass. In the calculation, we assume the stellar wind from the primary to be isotropic, and utilize the wind velocities numerically given in table A.7 of Hainich et al., 2020 as a function of the distance from the star, which is assumed to have a radius of 16.5 $R_\odot$. We adopt $\dot{M}_{\rm acc} = 3 \times 10^{-8} M_\odot$ yr^{-1} from Hainich et al., 2020. The orbital motion of the NS is calculated using the orbital period of equation (5.1), together with three cases for the primary's mass and the orbital eccentricity as described in the caption. The X-ray conversion factor is set to be unity, i.e., the gravitational energy gained via accretion is all converted to the radiation, assuming a NS radius of 12 km and a NS mass of 1.4 $M_\odot$. Any other complex effects (e.g., a photoionization of the stellar wind by the X-ray) are not taking into account in this calculation.

The X-ray luminosity changes calculated in this way are superposed in figure 6.1 on the observed data, where the phase 0 is aligned with the periastron passage time of equation (2). The model curves have the peak at an orbital phase of 0.02–0.03, This is because $v_{\rm rel}$ becomes minimum right after the periastron passage as shown in figure 6.3d. In contrast, the observed luminosity peak is more delayed from the periastron epoch. As already mentioned in subsection 6.2, this discrepancy may be attributed to some anisotropy of the stellar wind properties. We do not discuss this issue any further.

The calculated orbital modulation of the luminosity is thus 1.5 to 2.5 orders of magnitude, which arises mainly due to changes in $v_{\rm rel}$, hence those in $R_{\rm cap}$, along the eccentric orbit. These are significantly smaller than the observed dynamic range (3 orders of magnitude). Even when a systematic normalization adjustment (due, e.g., to an estimation error of $\dot{M}_{\rm w}$) is allowed between the observation and calculation, this discrepancy is too large to be attributed to systematic errors of any of the assumed parameters. For example, to explain the observation, the orbital eccentricity would have to be extremely large as > 0.9, in contradiction to the optical observations. Alternatively, the stellar winds should have to be accelerated to have a twice higher velocity at the apastron than at the periastron; this is also unlikely. A still more important point is that none of these ideas would be able to explain the markedly dim phase interval observed between the orbital phases of ~ 0.3 and ~ 0.95. To explain this phenomenon, we need to invoke some additional effects, in addition to the simple Hoyle-Lyttleton accretion scenario.

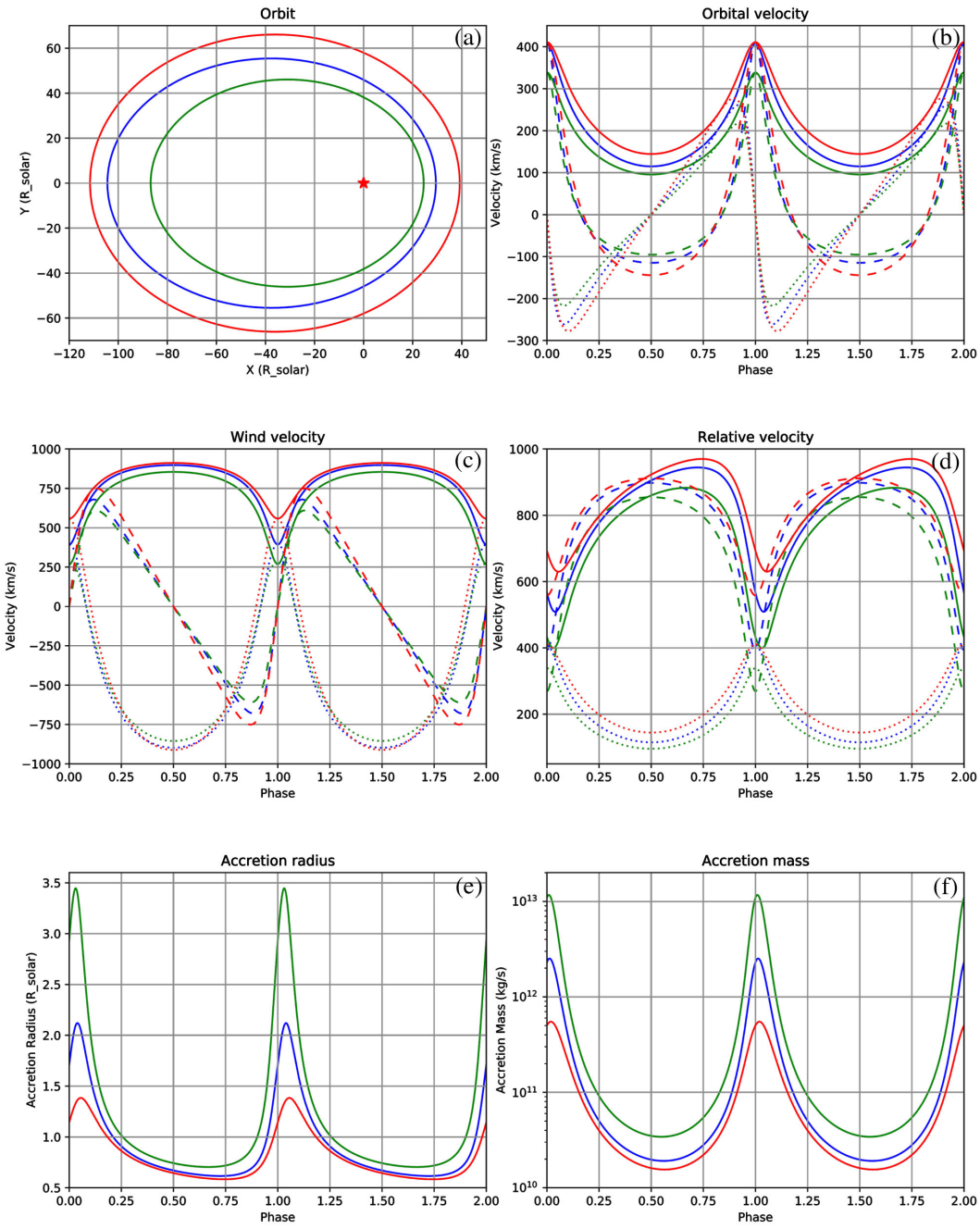

FIGURE 6.3: Intermediate output for figure 6.1. The line colors indicate the same as in figure 6.1. (a) NS's orbital in the rest frame for the massive star. (b)-(c) The orbital velocity and the wind velocity are plotted for the orbital phase. The dashed, dotted, and solid lines indicate the x-axis component, the y-axis component, and the magnitude of the velocity vectors, respectively. (d) The solid lines indicate the relative velocity of orbital velocity and wind velocity. The dashed and dotted lines are the same as the solid lines in panel (b)-(c). (e) The accretion radii for the orbital phase. (f) The resultant accretion mass for the orbital phase.

One possibility is the X-ray photoionization of the stellar winds, which may cause large luminosity changes along the orbit (Bozzo, Ducci, and Falanga, 2020). To evaluate this effect, we calculated the ionization parameter ξ at the periastron. Among the three conditions considered in the present work, the shortest distance between the primary's surface and the NS is $r \sim 10\ R_\odot$, where the stellar-wind density becomes $n \sim 10^{11}$ cm^{-3} (Hainich et al., 2020). The maximum X-ray luminosity is $L \sim 10^{36}$ erg s^{-1}. These conditions yield $\xi \equiv L/nr^2 \sim 20$ erg s^{-1} cm^{-1}. Therefore, the photoionization would not work sufficiently in IGR J00370+6122, because it is considered inefficient even in Vela X-1, which has a much higher value of $\xi \sim 10^4$ (Bozzo, Ducci, and Falanga, 2020). Even if the photoionization ever worked, it would produce two sharp peaks in the orbital X-ray light curve (Bozzo, Ducci, and Falanga, 2020), one preceding and the other following the periastron, with a relatively reduced luminosity in between. The observed behavior of IGR J00370+6122 is opposite, showing an abrupt luminosity increase over an orbital phase near the periastron between ∼0.3 and 0.95. Therefore, we conclude that the photoionization effect cannot explain the light curve of this system, and that other explanations must be sought for.

The observed long pulse period and the low X-ray luminosity make IGR J00370+6122 very reminiscent of X-Persei, which has $B \sim 10^{14}$ G (see section 1). Similarly, comparing three fundamental radii of accreting NS binaries, i.e. accretion, corotation, and Alfvén radii, Grunhut, Bolton, and McSwain, 2014 argued that IGR J00370+6122 possibly has a strong MF of $\sim 10^{15}$ G. If so, we naturally expect the operation of so-called propeller effect, which has actually been observed in some NS binaries (e.g., Asai et al., 2013; Tsygankov et al., 2016). In short, the gravitationally captured material can accrete onto the NS (accretion mode) when the matter density is high and hence the Alfvén radius is smaller than the co-rotation radius. When the matter density decreases to below a certain threshold, the pulsar magnetosphere will expand beyond the co-rotation radius, to prevent the direct mass accretion onto the NS. The latter is often called "propeller mode", because the rotating magnetosphere would expel the matter off the NS. This picture can explain the very low luminosity away from the periastron as a continued propeller-mode phase, and the observed luminosity jumps as the epochs of transitions between the accretion and propeller modes. This inference is strengthened by the histograms given on the right side of figure 6.1, which indicate that the luminosity takes a bimodal distribution, with a gap between $\sim 10^{33}$ and $\sim 10^{34}$ erg s^{-1}.

Let us apply the propeller effect modeling to the case of IGR J00370+6122. If the transition between the accretion mode and the propeller mode takes place at an X-ray luminosity $L_{\rm X}$, where the gravitational pull and the magnetic pressure are balanced, the dipolar MF strength B (expressed by its value on the surface) is given as

$$B \sim 5.7 \times 10^{13} \zeta^{-\frac{7}{4}} \left(\frac{L_{\rm X}}{10^{33}\ {\rm erg\ s^{-1}}} \right)^{\frac{1}{2}} \left(\frac{P}{10^3\ {\rm s}} \right)^{\frac{7}{6}} \quad {\rm G} \tag{6.3}$$

where P is the spin period and $\zeta \sim 1$ is a numerical factor (Makishima, 2016). Employing $P = 674$ s and the mode transition luminosity as $\sim 2 \times 10^{33}$ erg s^{-1} from figure 6.1, we obtain $B \sim 5 \times 10^{13}$ G. As clear from the above equation, this high value of B is a direct consequence of the long spin period. In addition, the very low luminosity of IGR J00370+6122 can be explained naturally as a consequence of magnetic inhibition of the wind capture process (Yatabe et al., 2018). Thus, IGR J00370+6122, like X Persei, is thought to have a dipole MF which is considerably higher than those of typical binary X-ray pulsars, and is even comparable to those of magnetars. This inference agrees with the suggestion derived in subsection 6.2 based

on our broadband spectral comparison. In this case, the CRSF should appear around 600 keV, which would be hard to detect. This is consistent with an apparent lack of the CRSF in the 1–80 keV spectrum of figure 6.2.

We have so far invoked the GL79 torque equilibrium theory and a strong MF to explain the low luminosity and the slow spin period. The application of the GL79 scheme is supported by a series of successful calibrations (see Introduction), and the case of the two Be-type pulsars, 4U 0115+63 (3.6 s pulse period) and X0331+53 (V0332+53, 4.4 s). In a declining phase of their outbursts, these objects showed a clear luminosity drop, to be interpreted as due to the propeller effect (Tsygankov et al., 2016), at luminosities of 1.4×10^{36} erg s^{-1} and 2.0×10^{36} erg s^{-1}, respectively. Then, equation (6.3) gives $B = 3.0 \times 10^{12} \zeta^{-\frac{7}{4}}$ G for 4U 0115+63 and $B = 4.5 \times 10^{12} \zeta^{-\frac{7}{4}}$ G for X0331+53, which agree very well with their surface MF strength measured with the CRSF, 1.2×10^{12} G and 3.0×10^{12} G, respectively (Makishima, 2016). Of course, some reservations may be needed, because the presence of a stable accretion disk, assumed in the GL79 scheme, may not necessarily be applicable to the present object. If, instead, QSA which we explained in section 1.4.3 takes place, the required MF strength would be reduced to $\sim 10^{12}$ G (e.g., Sanjurjo-Ferrrín et al., 2017). For example, the SFXT IGR J11215−5952 is very reminiscent of IGR J00370+6122. Sidoli et al. (2020) tried to explain its behavior using the QSA framework. In the present study, considering the richer observational verification of the GL79 scheme than that of the QSA, and the independent evidence from the harder and flatter spectral continuum, we would still favor the strong-MF interpretation of IGR J00370+6122.

We compared the observational facts for IGR J00370+6122 and IGR J11215−5952 in table 6.1. The CRSF is not reported for both objects in several 10s keV, and their

Table 6.1: Observational facts related to their surface MF for IGR J00370+6122 and IGR J11215−5952.

Object	CRSF	$E_{\rm fold}$ (keV)	$P_{\rm spin}$ (s)	$L_{\rm ave}^{[1]}$	$L_{\rm q}^{[2]}$	Orbital period (d)
J00370+6122	N/A	> 38.6	675	~ 1.0	~ 0.1	15.6649
J11215−5952[3]	N/A	~ 24	186.78	$\sim$9.0	$<$3.7	164.6

[1] Phase-averaged luminosity in units of 10^{35} erg s^{-1}.
[2] Luminosity in quiescent phases in units of 10^{33} erg s^{-1}.
[3] Parameters refer to Sidoli et al., 2020; Swank, Smith, and Markwardt, 2007; Romano et al., 2007; Romano et al., 2009.

MF is probably not the order of 10^{12} G. IGR J00370+6122 fulfills all of the features for highly-magnetized systems, i.e. high cutoff energy, slow spin period, constantly low luminosity, and large dynamic range. Then, we concluded that IGR J00370+6122 has the very strong MF of $\sim 5 \times 10^{13}$ G. Since IGR J11215−5952 has the ~ 4 times faster rotation period, the slightly higher luminosity and the lower folding energy, the MF of IGR J11215−5952 is thought to be weaker (but the same order) than that of IGR J00370+6122, assuming the same accretion rate (the companion star of IGR J11215−5952 is unknown). Sidoli et al. (2020) reported that IGR J11219−5952 had the very weak MF of $B = (0.1 - 10) \times 10^{12}$ G without discussing the stronger possibility of $\gg 10^{12}$ G. According to the similarity with IGR J00370+6122, we think that the MF of IGR J11215−5952 is probably as strong as $\sim 10^{13}$ G.

This conclusion will be strengthened if follow-up observations of IGR J00370+6122 in the future confirms the rapid luminosity jump at the orbital phases ~ 0.3 and ~ 0.95.

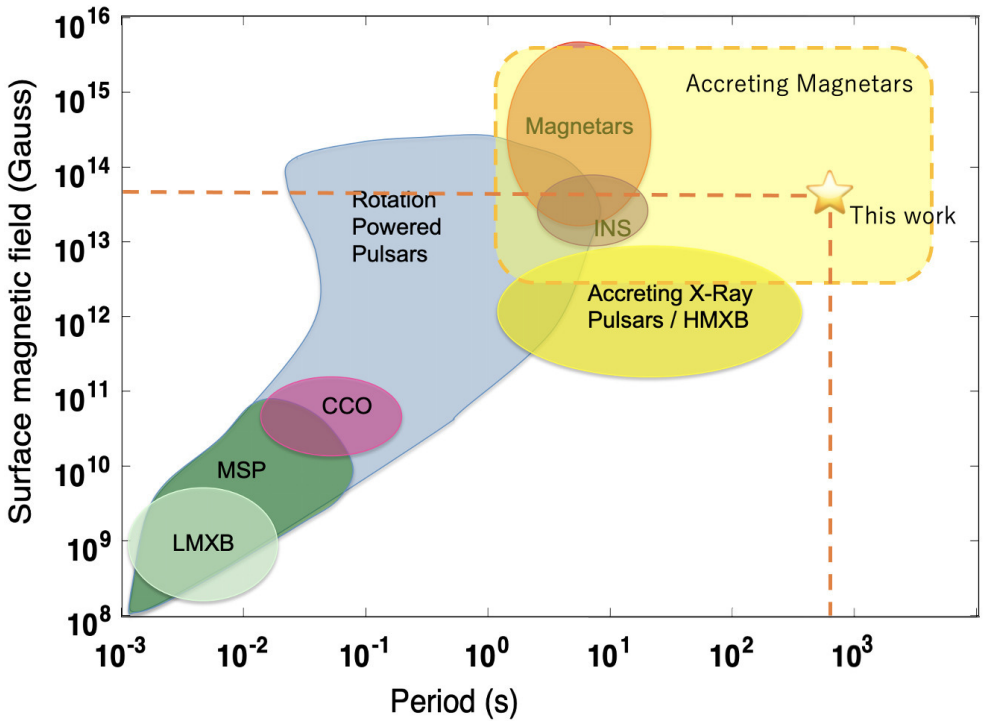

FIGURE 6.4: P-B diagram for know NS classifications. A original image is available in Harding, 2013. The marked star indicates the position of IGR J00370+6122.

6.4 Evolution of NSs and future perspectives

In the present study, we found the NS which preserves the magnetar-like strong MF in the HMXB by various observational results. The NS in IGR J00370+6122 can be an old-magnetar ($B_{\rm d} \sim 5 \times 10^{13}$ G) that is in the stage of decaying its MF from an original MF of $\sim 10^{15}$ G. This strongly supports an evolutionary theory that the magnetar can be born in binary systems not only as in solely. For isolated NSs, they emit X-rays by converting magnetic and/or rotational energy, and gradually spin down and lose their X-ray luminosity. In addition to the magnetic braking, NSs in binaries are spun down even more strongly by the propeller effect. An applicability of the GL79 model for a wind-fed HMXB, which is one of the facts newly found in this paper, can bring a dramatic change in the magnetar search in binary systems. This find will help us to pioneer a potential region in the NS zoo (i.e., top right in figure 6.4 (Harding, 2013)). The newest and future X-ray satellites, eROSITA and Einstein Probe, will survey all sky with the better sensitivity and find a lot of accretion magnetar with the GL79 model.

Chapter 7

Conclusion

By analyzing archival X-ray data of IGR J00370+6122 obtained with XMM-Newton, Suzaku, Swift, RXTE, and INTEGRAL, we have obtained the following results.

1. The orbital period has been refined. Near the periastron, the source brightens up to $\sim 2 \times 10^{35}$ erg s^{-1}, and often exhibits flaring activity. The luminosity peak is delayed by ~ 0.05 orbital cycles from the periastron passage.

2. From the 1st 8 ks of the 2008 XMM-Newton observation made near periastron, a possible periodicity was detected at 674 s. This strongly suggests that the compact object is an accreting magnetized NS rotating rather slowly at this period. Because the pulse profile folded at 674 s is double peaked, the previously reported 346 s period could be half (or twice in frequency) that observed in the present work.

3. Through the analysis of 1–10 keV spectra obtained with 3 instruments, the "harder when brighter"trend has been confirmed. This makes IGR J00370+6122 similar to known binary pulsars accreting at low luminosities.

4. A combined 10–80 keV spectrum can be described by a single power-law with $\Gamma \sim 2.2$ without noticeable cutoff. Its similarity to the spectrum of X Persei empirically suggests that IGR J00370+6122 has a considerably higher MF than ordinary X-ray pulsars.

5. Away from the periastron, the luminosity has been found to decrease by 3 orders of magnitude, down to $\sim 1 \times 10^{32}$ erg s^{-1}, involving abrupt luminosity jumps. These can be explained by the magnetic propeller effect, and a MF of 5×10^{13} G is derived.

In the present work, we applied the GL79 model newly for the wind-fed HMXB and derive the magnetar-like MF. The strong MF from the GL79 model is also supported by other observational results, i.e. the low luminosity, slow spin period, and the similarities of spectral shape with other highly-magnetized NSs. By examining the spectral shape and behavior in detail, we found that the X-ray emission region can be better explained by bremsstrahlung in the accretion column with low density rather than thermal radiation from a dense NS surface. We have shown that the GL79 model can be applied to the wind-fed HMXB, and this method will be utilized to find more accreting magnetars in the future.

Bibliography

Asai, K. et al. (Aug. 2013). "A PROPELLER-EFFECT INTERPRETATION OF MAXI/GSC LIGHT CURVES OF 4U 1608–52 AND Aql X-1 AND APPLICATION TO XTE J1701–462". In: *The Astrophysical Journal* 773.2, p. 117. DOI: 10.1088/0004-637x/773/2/117. URL: https://doi.org/10.1088/0004-637x/773/2/117.

Baade, W. and F. Zwicky (May 1934). "On Super-novae". In: *Proceedings of the National Academy of Science* 20.5, pp. 254–259. DOI: 10.1073/pnas.20.5.254.

Ballhausen, Ralf et al. (2017). "Looking at A 0535+26 at low luminosities with NuSTAR". In: *Astronomy & Astrophysics* 608, A105. DOI: 10.1051/0004-6361/201730845. URL: https://doi.org/10.1051/0004-6361/201730845.

Bozzo, E, L Ducci, and M Falanga (Dec. 2020). "A semi-analytical treatment to wind accretion in neutron star supergiant high-mass X-ray binaries âĂŞ I. Eccentric orbits". In: *Monthly Notices of the Royal Astronomical Society* 501.2, pp. 2403–2417. ISSN: 0035-8711. DOI: 10.1093/mnras/staa3761. eprint: https://academic.oup.com/mnras/article-pdf/501/2/2403/35392067/staa3761.pdf. URL: https://doi.org/10.1093/mnras/staa3761.

Bozzo, E., M. Falanga, and L. Stella (Aug. 2008). "Are There Magnetars in High-Mass X-Ray Binaries? The Case of Supergiant Fast X-Ray Transients". In: *The Astrophysical Journal* 683.2, pp. 1031–1044. DOI: 10.1086/589990. URL: https://doi.org/10.1086/589990.

Bradt, H. V., Rothschild, R. E., and Swank, J. H. (Jan. 1993). "X-ray timing explorer mission". In: *Astronomy & Astrophysics* 97.1, pp. 355–360.

Brown et al. (2018). "Gaia Data Release 2 - Summary of the contents and survey properties". In: *Astronomy & Astrophysics* 616, A1. DOI: 10.1051/0004-6361/201833051. URL: https://doi.org/10.1051/0004-6361/201833051.

Cash, Webster (1979). "PARAMETER ESTIMATION IN ASTRONOMY THROUGH APPLICATION OF THE LIKELIHOOD RATIO". In: *The Astrophysical Journal* 228, pp. 939–947.

Doroshenko, V. et al. (2012). "The hard X-ray emission of X Persei". In: *Astronomy & Astrophysics* 540, p. L1. DOI: 10.1051/0004-6361/201218878. URL: https://doi.org/10.1051/0004-6361/201218878.

Ducci, L. et al. (2013). "Swift/XRT orbital monitoring of the candidate supergiant fast X-ray transient IGR J17354-3255". In: *Astronomy & Astrophysics* 556, A72. DOI: 10.1051/0004-6361/201321635. URL: https://doi.org/10.1051/0004-6361/201321635.

Enoto, Teruaki, Shota Kisaka, and Shinpei Shibata (Oct. 2019). "Observational diversity of magnetized neutron stars". In: *Reports on Progress in Physics* 82.10, 106901, p. 106901. DOI: 10.1088/1361-6633/ab3def.

Enoto, Teruaki et al. (Apr. 2014). "Spectral and Timing Nature of the Symbiotic X-Ray Binary 4U 1954+319: The Slowest Rotating Neutron Star in an X-Ray Binary System". In: *The Astrophysical Journal* 786.2, p. 127. DOI: 10.1088/0004-637x/786/2/127. URL: https://doi.org/10.1088/0004-637x/786/2/127.

Faber, Joshua A and Frederic A Rasio (2012). "Binary Neutron Star Mergers". In: *Living Rev. Relativity* 15.8. ISSN: 1433-8351. URL: http://www.livingreviews.org/lrr-2012-8http://ccrg.rit.edu/people/faberhttp://ciera.northwestern.edu/rasio/.

Farinelli, R. et al. (Feb. 2012). "Numerical solution of the radiative transfer equation: X-ray spectral formation from cylindrical accretion onto a magnetized neutron star". In: *Astronomy & Astrophysics* 538, A67, A67. DOI: 10.1051/0004-6361/201118008. arXiv: 1111.6851 [astro-ph.HE].

Frank, J., A. R. King, and J. P. Lasota (May 1987). "The light curves of low-mass X-ray binaries." In: *Astronomy & Astrophysics* 178, pp. 137–142.

Fumio T. et al. (Feb. 2020). "Handbook of Astrophysics(宇宙物理学ハンドブック)". In: *Asakura Publishing Co., Ltd.*

Ghosh, P. and F. K. Lamb (Nov. 1979). "Accretion by rotating magnetic neutron stars. III - Accretion torques and period changes in pulsating X-ray sources". In: *The Astrophysical Journal* 234, p. 296. ISSN: 0004-637X. DOI: 10.1086/157498.

González-Galán, A. et al. (June 2014). "Astrophysical parameters and orbital solution of the peculiar X-ray transient IGR J00370+6122". In: *Astronomy & Astrophysics* 566, A131. ISSN: 0004-6361. DOI: 10.1051/0004-6361/201423554. URL: http://www.aanda.org/10.1051/0004-6361/201423554.

Grunhut, J. H., C. T. Bolton, and M. V. McSwain (Mar. 2014). "Orbit and properties of the massive X-ray binary BD+60 73=IGR J00370+6122". In: *Astronomy & Astrophysics* 563, A1. ISSN: 0004-6361. DOI: 10.1051/0004-6361/201322738. URL: http://www.aanda.org/10.1051/0004-6361/201322738.

Hainich, R et al. (2020). "Astronomy The stellar and wind parameters of six prototypical HMXBs and their evolutionary status". In: *Astronomy & Astrophysics*. DOI: 10.1051/0004-6361/201935498. URL: https://doi.org/10.1051/0004-6361/201935498.

Harding, Alice K. (Dec. 2013). "The neutron star zoo". In: *Frontiers of Physics* 8.6, pp. 679–692. DOI: 10.1007/s11467-013-0285-0. arXiv: 1302.0869 [astro-ph.HE].

Harrison, Fiona A. et al. (May 2013). "THE NUCLEAR SPECTROSCOPIC TELESCOPE ARRAY (NuSTAR) HIGH-ENERGY X-RAY MISSION". In: *The Astrophysical Journal* 770.2, p. 103. DOI: 10.1088/0004-637x/770/2/103. URL: https://doi.org/10.1088/0004-637x/770/2/103.

Hartog, P. R den et al. (May 2004). "IGR J00370+6122 - A new high-mass X-ray binary". In: *The Astronomer's Telegram* 281.281. URL: http://www.astronomerstelegram.org/?read=281.

Hoyle, F. and R. A. Lyttleton (1939). "The effect of interstellar matter on climatic variation". In: *Mathematical Proceedings of the Cambridge Philosophical Society* 35.3, pp. 405–415. DOI: 10.1017/S0305004100021150.

in 't Zand, J. J. M. et al. (July 2007). "A probable accretion-powered X-ray pulsar in IGR J00370+6122". In: *Astronomy & Astrophysics* 469.3, pp. 1063–1068. ISSN: 0004-6361. DOI: 10.1051/0004-6361:20077189. URL: http://www.aanda.org/10.1051/0004-6361:20077189.

Israel, G. L. and L. Stella (Sept. 1996). "A New Technique for the Detection of Periodic Signals in "Colored" Power Spectra". In: *The Astrophysical Journal* 468, p. 369. DOI: 10.1086/177697. arXiv: astro-ph/9603038 [astro-ph].

Koliopanos, Filippos and Vasilopoulos, Georgios (2018). "Accreting, highly magnetized neutron stars at the Eddington limit: a study of the 2016 outburst of SMC X-3". In: *Astronomy & Astrophysics* 614, A23. DOI: 10.1051/0004-6361/201731623. URL: https://doi.org/10.1051/0004-6361/201731623.

Krimm, H. A. et al. (Oct. 2013). "THE SWIFT BAT HARD X-RAY TRANSIENT MONITOR". In: *The Astrophysical Journal Supplement* 209.1, p. 14. DOI: 10.1088/0067-0049/209/1/14. URL: https://doi.org/10.1088/0067-0049/209/1/14.

Makishima, K. et al. (Nov. 1999). "Cyclotron Resonance Effects in Two Binary XRay Pulsars and the Evolution of Neutron Star Magnetic Fields". In: *The Astrophysical Journal* 525.2, pp. 978–994. ISSN: 0004-637X. DOI: 10.1086/307912. URL: https://iopscience.iop.org/article/10.1086/307912https://iopscience.iop.org/article/10.1086/307912/meta.

Makishima, Kazuo (Apr. 2016). *X-ray studies of neutron stars and their magnetic fields*. DOI: 10.2183/PJAB.92.135.

Makishima, Kazuo et al. (June 2008). "Suzaku Results on Cygnus X-1 in the Low/Hard State". In: *Publications of the Astronomical Society of Japan* 60.3, pp. 585–604. ISSN: 0004-6264. DOI: 10.1093/pasj/60.3.585. eprint: https://academic.oup.com/pasj/article-pdf/60/3/585/17453047/pasj60-0585.pdf. URL: {https://doi.org/10.1093/pasj/60.3.585}.

Matsuoka, Masaru and Kazumi Asai (Apr. 2013). "Simplified Picture of Low-Mass X-Ray Binaries Based on Data from Aquila X-1 and 4U 1608âĂŞ52". In: *Publications of the Astronomical Society of Japan* 65.2. 26. ISSN: 0004-6264. DOI: 10.1093/pasj/65.2.26. eprint: https://academic.oup.com/pasj/article-pdf/65/2/26/9718002/pasj65-0026.pdf. URL: https://doi.org/10.1093/pasj/65.2.26.

Mcclintock, J E et al. (June 1976). "DISCOVERY OF A 283-SECOND PERIODIC VARIATION IN THE X-RAY SOURCE 3U 0900-40". In: *The Astrophysical Journal* 206, pp. 99–102.

Mihara, T. et al. (July 1990). "New observations of the cyclotron absorption feature in Hercules X-1". In: *Nature* 346.6281, pp. 250–252. DOI: 10.1038/346250a0.

Mihara, Tatehiro (June 1995). "Observational Study of X-ray spectra of Binary Pulsars with Ginga". PhD thesis. University of Tokyo.

Mitsuda, Kazuhisa et al. (Jan. 2007). "The X-Ray Observatory Suzaku". In: *Publications of the Astronomical Society of Japan* 59.sp1, S1–S7. ISSN: 0004-6264. DOI: 10.1093/pasj/59.sp1.S1. eprint: https://academic.oup.com/pasj/article-pdf/59/sp1/S1/17451491/pasj59-00S1.pdf. URL: https://doi.org/10.1093/pasj/59.sp1.S1.

Morgan, W. W., A. D. Code, and A. E. Whiteford (May 1995). "STUDIES IN GALACTIC STRUCTURE. II. LUMINOSITY CLASSIFICATION FOR 1270 BLUE GIANT STARS". In: *The Astrophysical Journal Supplement* 2, p. 41.

Nagase, F. (Jan. 1989). "Accretion-powered X-ray pulsars." In: *Publications of the Astronomical Society of Japan* 41, p. 1.

Ohsugi, Y. (2018). "Bondi-Hoyle-Lyttleton accretion flow revisited: Numerical simulation of unstable flow". In: *Astronomy and Computing* 25, pp. 44–51. ISSN: 2213-1337. DOI: https://doi.org/10.1016/j.ascom.2018.08.005. URL: https://www.sciencedirect.com/science/article/pii/S2213133716301378.

Ono, Ko et al. (Apr. 2017). "A hard-to-soft state transition of Aquila X-1 observed with Suzaku". In: *Publications of the Astronomical Society of Japan* 69.2, 23, p. 23. DOI: 10.1093/pasj/psw126. arXiv: 1612.04924 [astro-ph.HE].

Raguzova, Natalya V and Vladimir M Lipunov (1998). "High-eccentric X-ray binaries: evolution, wind rose effect, accretor-propeller luminosity gap". In: *Astronomy & Astrophysics* 340, pp. 85–102.

Reig, P. et al. (Sept. 2005). "Identification of the optical counterparts of high-mass X-ray binaries through optical photometry and spectroscopy". In: *Astronomy &*

Astrophysics 440.2, pp. 637–646. ISSN: 0004-6361. DOI: 10.1051/0004-6361:20052684. URL: http://www.aanda.org/10.1051/0004-6361:20052684.

Reig, P. and Nespoli, E. (2013). "Patterns of variability in Be/X-ray pulsars during giant outbursts". In: *Astronomy & Astrophysics* 551, A1. DOI: 10.1051/0004-6361/201219806. URL: https://doi.org/10.1051/0004-6361/201219806.

Revnivtsev, M. et al. (2003). "The spectrum of the cosmic X-ray background observed by RTXE/PCA". In: *Astronomy & Astrophysics* 411.3, pp. 329–334. DOI: 10.1051/0004-6361:20031386. URL: https://doi.org/10.1051/0004-6361:20031386.

Romano, P. et al. (July 2007). "Swift/XRT observes the fifth outburst of the periodic supergiant fast X-ray transient IGR J11215-5952". In: *Astronomy & Astrophysics* 469.1, pp. L5–L8. DOI: 10.1051/0004-6361:20077383. arXiv: 0704.0543 [astro-ph].

Romano, P. et al. (May 2009). "Disentangling the System Geometry of the Supergiant Fast X-Ray Transient IGR J11215-5952 with Swift". In: *The Astrophysical Journal* 696.2, pp. 2068–2074. DOI: 10.1088/0004-637X/696/2/2068. arXiv: 0902.1985 [astro-ph.HE].

Romano, P. et al. (Jan. 2010). "Swift/XRT monitoring of the supergiant fast X-ray transient IGR J18483 − 0311 for an entire orbital period". In: *Monthly Notices of the Royal Astronomical Society* 401.3, pp. 1564–1569. ISSN: 0035-8711. DOI: 10.1111/j.1365-2966.2009.15789.x. eprint: https://academic.oup.com/mnras/article-pdf/401/3/1564/3810869/mnras0401-1564.pdf. URL: https://doi.org/10.1111/j.1365-2966.2009.15789.x.

Romano, P. et al. (Jan. 2012). "Swift/X-ray Telescope monitoring of the candidate supergiant fast X-ray transient IGR J16418 − 4532". In: *Monthly Notices of the Royal Astronomical Society* 419.3, pp. 2695–2702. ISSN: 0035-8711. DOI: 10.1111/j.1365-2966.2011.19916.x. eprint: https://academic.oup.com/mnras/article-pdf/419/3/2695/18720108/mnras0419-2695.pdf. URL: https://doi.org/10.1111/j.1365-2966.2011.19916.x.

Sanjurjo-Ferrrín, G. et al. (Oct. 2017). "XMM-Newton spectroscopy of the accreting magnetar candidate 4U0114+65". In: *Astronomy & Astrophysics* 606, A145, A145. DOI: 10.1051/0004-6361/201630119. arXiv: 1706.04907 [astro-ph.HE].

Santangelo, A. et al. (Sept. 1999). "A BEPPOSAX Study of the Pulsating Transient X0115+63: The First X-Ray Spectrum with Four Cyclotron Harmonic Features". In: *The Astrophysical Journal* 523.1, pp. L85–L88. DOI: 10.1086/312249. URL: https://doi.org/10.1086/312249.

Sasano, Sasano (Dec. 2014). "X-ray Studies of Highly Magnetized Neutron Stars in Binary Systems with Suzaku". PhD thesis. University of Tokyo.

Sidoli, L. (June 2017). "Supergiant Fast X-ray Transients - A short review". In: *XII Multifrequency Behaviour of High Energy Cosmic Sources Workshop (MULTIF2017)*, p. 52. arXiv: 1710.03943 [astro-ph.HE].

Sidoli, L. et al. (June 2020). "NuSTAR observation of the supergiant fast X-ray transient IGR J11215-5952 during its 2017 outburst". In: *Astronomy & Astrophysics* 638, A71, A71. DOI: 10.1051/0004-6361/202038078. arXiv: 2004.10452 [astro-ph.HE].

Sugizaki, Mutsumi et al. (Aug. 2015). "Luminosity and spin-period evolution of GX 304-1 during outbursts from 2009 to 2013 observed with the MAXI/GSC, RXTE/PCA, and Fermi/GBM". In: *Publications of the Astronomical Society of Japan* 67.4, 73, p. 73. DOI: 10.1093/pasj/psv039. arXiv: 1504.04895 [astro-ph.HE].

Sugizaki, Mutsumi et al. (2017). "Correlation between the luminosity and spin-period changes during outbursts of 12 Be binary pulsars observed by the MAXI/GSC and the Fermi/GBM". In: *Publications of the Astronomical Society of Japan* 69.6, pp. 100–101. DOI: 10.1093/pasj/psx119. URL: http://gammaray.nsstc.nasa.gov/gbm/science/pulsars/..

Sugizaki, Mutsumi et al. (June 2020). "X-Ray Emission Evolution of the Galactic Ultraluminous X-Ray Pulsar Swift J0243.6+6124 during the 2017-2018 Outburst Observed by the MAXI GSC". In: *The Astrophysical Journal* 896.2, 124, p. 124. DOI: 10.3847/1538-4357/ab93c7. arXiv: 2005.07971 [astro-ph.HE].

Swank, J. H., D. M. Smith, and C. B. Markwardt (Feb. 2007). "RXTE PCA Pointed Observations of IGR J11215-5952". In: *The Astronomer's Telegram* 999, p. 1.

Takagi, Toshihiro et al. (June 2016). "Application of the Ghosh & Lamb relation to the spin-up/down behavior in the X-ray binary pulsar 4U 1626-67". In: *Publications of the Astronomical Society of Japan* 68, S13, S13. DOI: 10.1093/pasj/psw010. arXiv: 1601.04894 [astro-ph.HE].

Takahashi, Hiromitsu, Soki Sakurai, and Kazuo Makishima (Sept. 2011). "Rossi X-ray Timing Explorer Observations of the Low-mass X-ray Binary 4U 1608-522 in the Upper-banana State". In: *The Astrophysical Journal* 738.1, 62, p. 62. DOI: 10.1088/0004-637X/738/1/62. arXiv: 1107.3603 [astro-ph.HE].

Terada, Y. et al. (2007). "Suzaku observations of cyclotron resonances in binary X-ray pulsars". In: *Advances in Space Research* 40.10, pp. 1485–1490. ISSN: 0273-1177. DOI: https://doi.org/10.1016/j.asr.2007.02.020. URL: https://www.sciencedirect.com/science/article/pii/S0273117707001068.

Truemper, J. et al. (Feb. 1978). "Evidence for strong cyclotron line emission in the hard X-ray spectrum of Hercules X-1." In: *The astrophysical journal letters* 219, pp. L105–L110. DOI: 10.1086/182617.

Tsygankov, S. S. et al. (Aug. 2016). "Propeller effect in two brightest transient X-ray pulsars: 4U 0115+63 and V 0332+53". In: *Astronomy & Astrophysics* 593, A16, A16. DOI: 10.1051/0004-6361/201628236. arXiv: 1602.03177 [astro-ph.HE].

Tsygankov, Sergey S. et al. (July 2019a). "Cyclotron emission, absorption, and the two faces of X-ray pulsar A 0535+262". In: *Monthly Notices of the Royal Astronomical Society* 487.1, pp. L30–L34. DOI: 10.1093/mnrasl/slz079.

Tsygankov, Sergey S. et al. (Feb. 2019b). "Dramatic spectral transition of X-ray pulsar GX 304-1 in low luminous state". In: *Monthly Notices of the Royal Astronomical Society* 483.1, pp. L144–L148. DOI: 10.1093/mnrasl/sly236.

Walter, Roland et al. (2011). "INTEGRAL in HEAVENS". In: *Proceedings of science* INTEGRAL 2010, p. 162. DOI: 10.22323/1.115.0162.

Wei, Dennis (2006). "X-ray power density spectra of black hole binaries : a new deadtime model for the RXTE PCA". In:

Wijnands, R. and N. Degenaar (Nov. 2016). "Meta-stable low-level accretion rate states or neutron star crust cooling in the Be/X-ray transients V0332+53 and 4U 0115+63". In: *Monthly Notices of the Royal Astronomical Society* 463.1, pp. L46–L50. DOI: 10.1093/mnrasl/slw096. arXiv: 1602.02275 [astro-ph.HE].

Yatabe, Fumiaki et al. (Oct. 2018). "An application of the Ghosh & Lamb model to the accretion-powered X-ray pulsar X Persei". In: *Publications of the Astronomical Society of Japan* 70.5. ISSN: 2053051X. DOI: 10.1093/pasj/psy088.